# DEVELOPMENT OF A NON-ORDINARY STATE-BASED PERIDYNAMICS SOLVER

A THESIS SUBMITTED TO
THE GRADUATE SCHOOL OF ENGINEERING AND SCIENCE
OF BILKENT UNIVERSITY
IN PARTIAL FULFILLMENT OF THE REQUIREMENTS FOR
THE DEGREE OF
MASTER OF SCIENCE
IN
MECHANICAL ENGINEERING

By
Rico Morasata
September 2019

DEVELOPMENT OF A NON-ORDINARY STATE-BASED PERIDYNAMICS SOLVER
By Rico Morasata
September 2019

We certify that we have read this thesis and that in our opinion it is fully adequate, in scope and in quality, as a thesis for the degree of Master of Science.

Ali Javili(Advisor)

Onur Özcan

Ercan Gürses

Approved for the Graduate School of Engineering and Science:

Ezhan Karaşan
Director of the Graduate School

# ABSTRACT

# DEVELOPMENT OF A NON-ORDINARY STATE-BASED PERIDYNAMICS SOLVER

Rico Morasata
M.S. in Mechanical Engineering
Advisor: Ali Javili
September 2019

Damage prediction is crucial in the design process of engineering structures to ensure structural integrity. The limitations of empirical methods and the high costs associated with experimental analyses have prompted the development of numerical methods to predict the initiation and/or propagation of cracks under prescribed loading conditions. While various methods exist for failure prediction, their formulations rely on partial differential equations with spatial derivatives. As a result, these methods require special treatments in order to accurately capture the underlying failure mechanisms. To overcome these limitations, the peridynamic theory has been introduced as a novel, nonlocal continuum formulation. In contrast to the other methods, it is expressed as an integro-differential equation devoid of spatial derivatives, hence applicable to structural analyses involving discontinuities. This project aims to elaborate on the development of a solver based on a specific variant of the peridynamic formulation to investigate the behavior of two- and three-dimensional structures under certain loading conditions. The current code is developed to solve quasi-static problems related to damage initiation and propagation. In addition, it is aimed to show that peridynamics can capture local, hyperelastic deformations. The overall structure of the code is reviewed and the potential extensions of the current work are discussed.

*Keywords:* Damage Prediction, Peridynamics, Cracks, Nonlocal Continuum Formulation.

# ÖZET

# TİPİK OLMAYAN DURUM BAZLI PERİDİNAMİK YÖNTEMİ ÇÖZÜCÜSÜNÜN GELİŞTİRİLMESİ

Rico Morasata
Makine Mühendisliği, Yüksek Lisans
Tez Danışmanı: Ali Javili
Eylül 2019

Hasar tahmini mühendislik yapılarının tasarım sürecinde yapısal bütünlüğü sağlamak için kritiktir. Ampirik yöntemlerin sınırlamaları ve deneylerin yüksek maliyetleri yüzünden, çatlakların başlatması ve/veya yayılmasını verilen yükleme koşulların altında tahmin edebilmek için, sayısal yöntemlerin geliştirmesi teşvik edilmiştir. Hasar tahmini için çeşitli yöntemler mevcut olmasına rağmen, onların formülasyonları gerilme tensörün bileşenlerin türevleri ile kısmi diferansiyel denklemlere dayanır. Bu sınırlamaları atlatmak için, peridinamik teorisi yeni yerel olmayan bir denklem olarak tanıtılmıştır. Diğer yöntemlerin aksine, gerilme tensörün bileşenlerin türevlerini içermeyen bir integro-diferansiyel denklem olarak ifade edilmiştir. Bu yüzden süreksizlikler içeren yapısal analizlere uygulanabilir. Bu projenin amacı iki ve üç boyutlu yapıların öngörülen yükleme koşulları altında davranışlarını araştırmak için, peridinamik yöntemin spesifik bir çeşitine dayanan bir çözücünün geliştirilmesini açıklamaktır. Mevcut kod hasar başlatması ve yayılması ile ilgili statik problemleri çözmek için geliştirilmiştir. Ve, mevcut yöntemin yerel deformasyonların yakalabileceği gösterilmiştir. Kodun genel yapısı gözden geçilir ve mevcut çalışmanın potansiyel uzantıları tartışılmıştır.

*Anahtar sözcükler*: Hasar tahmini, *Peridynamics*, Çatlaklar, *Nonlocal Continuum* Formülasyonu .

# Acknowledgement

First, I would like to express my deepest gratitude to Dr. Ali Javili for the opportunity to work on Peridynamics, his guidance, support and patience throughout my research. Working on Peridynamics has stimulated my interest in Computational Solid Mechanics, especially Multiscale Modeling.

Furthermore, I would like to address my special thanks to Dr. Erkan Oterkus at the University of Strathclyde for the numerous discussions we had regarding the peridynamic theory and the associated computational procedures.

Moreover, I am highly indebted to Dr. David Littlewood at Sandia National Laboratories for his valuable insight into the crucial components of a peridynamics solver, to Dr. Patrick Diehl of the Center for Computation & Technology at the Louisiana State University for his valuable guidance and to Mr. Michael Brothers at FutureWei Technologies for his insight into the implicit time integration in peridynamics.

Also, I would like to thank Dr. Cevdet Aykanat of the Computer Engineering Department at Bilkent University for his suggestions regarding the choice of algorithms and data structures which are central to the solver development.

I would like to acknowledge my friends at the Graduate Student Office for the moments we shared. Specifically, I am thankful to Mr. Onur Vardar for our frequent discussions regarding object-oriented programming, libraries and sparse matrix operations.

Last but not least, my deepest gratitude goes out to my parents, Léontine and Jacquot, and my brothers, Teddy and Kevin, for their lifelong, consistent support; I would not have reached this far without their encouragement.

# Contents

# List of Figures

# List of Tables

# Nomenclature

## Abbreviations

| Symbol | Description |
|---|---|
| BB-PD | Bond-Based Peridynamics |
| BC | Boundary Condition |
| CCM | Classical Continuum Mechanics |
| CSR | Compressed Sparse Row |
| DBC | Dirichlet Boundary Condition |
| DOF | Degree Of Freedom |
| FEM | Finite Element Method |
| IFD | Internal Force Density |
| LEFM | Linear Elastic Fracture Mechanics |
| LPS | Linear Peridynamic Solid |
| NOSB-PD | Non-Ordinary State-Based Peridynamics |
| OSB-PD | Ordinary State-Based Peridynamics |
| PD | Peridynamics |
| PMB | Prototype Microelastic Brittle |

| | |
|---|---|
| SB-PD | State-Based Peridynamics |
| SED | Strain Energy Density |
| TSM | Tangent Stiffness Matrix |
| XFEM | eXtended Finite Element Method |

## Symbols

| **Symbol** | **Description** | **Unit** |
|---|---|---|
| $\alpha$ | thermal expansion coefficient | $\mathrm{K}^{-1}$ |
| $\Delta$ | nodal spacing (uniform discretization) | m |
| $\delta$ | horizon | m |
| $\kappa$ | bulk modulus | $\mathrm{N/m}^2$ |
| $\lambda\,,\mu$ | Lamé constants | $\mathrm{N/m}^2$ |
| $\mu$ | history-dependent, scalar-valued function | |
| $\omega$ | influence function | |
| $\rho$ | density | $\mathrm{kg/m}^3$ |
| $\theta$ | dilatation | |
| $\underline{\boldsymbol{M}}$ | unit vector state in OSB-PD | |
| $\underline{\boldsymbol{T}}$ | force vector state | $\mathrm{N/m}^6$ |
| $\underline{\boldsymbol{t}}$ | scalar force state in OSB-PD | $\mathrm{N/m}^6$ |
| $\underline{\boldsymbol{X}}$ | initial deformation state of $\boldsymbol{x}$ | m |
| $\underline{\boldsymbol{Y}}$ | current deformation state of $\boldsymbol{x}$ | m |
| $\varphi$ | local damage index | |

| | | |
|---|---|---|
| $c$ | bond constant in BB-PD | $\mathrm{N/m^6}$ |
| $G_c$ | critical energy release rate | $\mathrm{J/m^2}$ |
| $m$ | horizon-to-grid-spacing ratio | |
| $s$ | bond stretch | |
| $s_c$ | critical stretch | |
| $\boldsymbol{\eta}$ | relative displacement vector | m |
| $\boldsymbol{\sigma}$ | Cauchy stress tensor | $\mathrm{N/m^2}$ |
| $\boldsymbol{\xi}$ | peridynamic bond | m |
| $\boldsymbol{C}$ | micromodulus tensor | |
| $\boldsymbol{E}$ | Green-Lagrange strain tensor | |
| $\boldsymbol{F}$ | approximate deformation gradient tensor | |
| $\boldsymbol{I}$ | second-order identity tensor | |
| $\boldsymbol{K}$ | shape tensor | |
| $\boldsymbol{P}$ | Piola stress tensor | |
| $\boldsymbol{u'}$ | displacement of $\boldsymbol{x'}$ | m |
| $\boldsymbol{u}$ | displacement of $\boldsymbol{x}$ | m |
| $\boldsymbol{x'}$ | position of a neighbor of $\boldsymbol{x}$ in the reference configuration/a neighbor of $\boldsymbol{x}$ | m |
| $\boldsymbol{x}$ | material point (its position in the reference configuration) | m |
| $\boldsymbol{y'}$ | position of $\boldsymbol{x'}$ in the current configuration | m |
| $\boldsymbol{y}$ | position of $\boldsymbol{x}$ in the current configuration | m |

| | |
|---|---|
| $\mathcal{B}$ | continuum body |
| $\mathcal{H}$ | neighborhood of a material point |

# Chapter 1

# Introduction

## 1.1 Fracture Mechanics Overview

Prediction of material damage and failure by means of numerical simulations remains a challenge in Computational Mechanics. Numerical methods for structural analysis are essentially based on the governing equations of Classical Continuum Mechanics (CCM) which are partial differential equations with spatial derivatives. As a result, difficulties emerge when the physical body under consideration contains discontinuities such as cracks. Inglis [1] proposed empirical relations to evaluate the stress concentrations in the vicinity elliptical holes using the linear elasticity theory. Since the latter assumes a continuous displacement field, these relations yield non-physical stress values at sharp crack tips. Aware of these results, Griffith [2] introduced an energy-based approach to predict fracture strength in brittle materials. His pioneering works laid the foundation of Linear Elastic Fracture Mechanics (LEFM). As noted in [3], LEFM is only applicable if the body under consideration has a pre-existing crack. Furthermore, crack growth requires the definition of external criteria. The application of LEFM into the Finite Element Method (FEM) necessitates special treatments such as remeshing the body after an incremental crack growth, so that the crack lies on element boundaries. In addition, the crack growth is defined *a priori* by means of a mathematical relation. These requirements affect the adequacy of the traditional FEM for practical applications involving cracks.

Various techniques have been developed to address these shortcomings including the cohesive zone concept [4, 5, 6], then the cohesive zone model (CZM) [7] as well the eXtended Finite Element Method (XFEM) [8] which is based on the concept of *partition of unity method* [9]. Nonetheless, these techniques have drawbacks: for the CZM, mesh quality significantly affects crack propagation and remeshing the body is necessary [10]. Although the XFEM allows for crack propagation across elements, it was observed that the method yields inaccurate solutions for problems involving complex crack interactions due to partial element enrichment around the crack tip [11]. Eringen [12] noted that the CCM formulation does not possess an internal length scale parameter that enables multiscale modeling. In contrast, due to the drastic differences in the associated length and time scales, Molecular Dynamics (MD) simulations are impractical for real-world problems at the macroscale. Consequently, nonlocal continuum theories have been introduced to account for long-range effects [13].

As indicated in [3], despite their ability to capture phenomena across different length scales, nonlocality in nonlocal theories is accounted for by means of strain averaging, i.e., their formulations still involve spatial derivatives, which is problematic when discontinuities are present in the domain.

To circumvent the difficulties associated with the aforementioned theories, Silling [14] introduced *peridynamics* as a novel continuum formulation, mathematically expressed as an integro-differential equation without spatial derivatives.

## 1.2 Aspects of the Peridynamics Theory

The first peridynamics (PD) formulation is referred to as *bond-based peridynamics* (BB-PD). Its fundamental assumption is that a continuum body is subdivided into infinitely many points of finite volume called *material points*, each of which interacts with those within its neighborhood through pairwise interactions of equal magnitude. As a result, several restrictions are imposed on material properties [3]. As a remedy, an improved version of the PD formulation called *state-based peridynamics* (SB-PD) has been introduced [15]. There are two main types of SB-PD formulations: *ordinary state-based peridynamics* (OSB-PD) and *non-ordinary state-based peridynamics* (NOSB-PD) formulations. In the OSB-PD formulation, the forces between the material points act along the same line of action but are of unequal magnitudes. In contrast, in the NOSB-PD formulation, the forces have different magnitudes and can act in arbitrary directions. Therefore, the NOSB-PD formulation encompasses the

BB-PD and OSB-PD formulations and is the main focus of the current work. Since its introduction, PD has been attractive to researchers across a plethora of disciplines. Recently, Javili et al. [16] identified the main applications of PD up to date in various domains. Upon examining the literature, it is noted that the main applications of PD are problems involving damage and failure prediction. These analyses are generally carried out using the BB-PD or the OSB-PD formulations. Notably, Liu et al. [17] developed a highly parallel, three-dimensional BB-PD code to simulate the behavior of ductile and brittle materials. Hu et al. [18] developed a BB-PD model to investigate progressive damage in composite laminates. Oterkus et al. [19] incorporated heat conduction within the OSB-PD framework and analyzed the deformation of pre-cracked structures subjected to thermal and mechanical loads.

It is worth mentioning that multiple material behaviors have been simulated by incorporating classical continuum models into the NOSB-PD formulation. In particular, Warren et al. [20] implemented an isotropic elastic–plastic linear hardening constitutive model to analyze three-dimensional structural deformations under transient dynamics. Foster et al. [21] extended their work and implemented a viscoplastic constitutive model within the peridynamic framework. Furthermore, the Johnson-Cook plasticity model has been incorporated into the NOSB-PD formulation in [22], then in the work of Amani et al. [23] in the context of thermoplastic fracture. Recently, Lai et al. [24] used the modified Johnson-Holmquist material model to analyze impact-induced fracture in quasi-brittle materials.

## 1.3 Motivation

Given the importance of damage prediction in structural design and the costs associated with experimental procedures, tremendous efforts have been dedicated to the development of robust and accurate numerical methods.

Recently, it is noted that there has been a growing interest in meshless methods for computational mechanics problems due to their flexibility in handling problems with large deformations and evolving discontinuities [25]. In contrast to the FEM which requires nodal connectivity, the discretization does not require an underlying structure but consists of nodes only; hence they are not affected by mesh distortion, mesh reconstruction and the challenges associated with the discretization of three-dimensional geometries [26, 25]. Among the most common meshless methods are the Smoothed Particle Hydrodynamics, the Reproducing Kernel Particle Method, the element-free Galerkin method and the Meshless Local Petrov-Galerkin method. In the literature, applications of meshless methods to solid mechanics problems include metal forming [27, 28], hyperelastic deformations [29], fracture modeling [30, 31].

Marder [32] reviewed the analytical theories and numerical simulations associated with the use of particle methods in fracture modeling. PD is described as “one of the first and certainly the best-developed particle method in which the particles are not atoms”. Indeed, PD has been successfully applied to a wide range of problems as shown in [16]. Furthermore, significant advances have been made in the numerical implementation of PD. The earliest contribution regarding the numerical implementation of PD is the code called EMU developed by Silling [33]. It is noted that Parks et al. [34] implemented PD within the MD code LAMMPS [35]. Macek and Silling [36] implemented the discretized BB-PD within the ABAQUS commercial finite element (FE) code. The authors emphasized the importance of a PD-FE coupling for damage prediction problems in terms of computational efficiency. To date, the most effective numerical implementation of PD is the open-source, massively parallel code Peridigm [37], developed by Sandia National Laboratories. It implements the OSB-PD and NOSB-PD formulations and has been used in numerous problems involving progressive damage, high-velocity impact and fragmentation. Also, the code may be extended to include custom constitutive models. Despite its remarkable features, the available documentation on user-defined material models is limited and the potential definition of user-defined damage models has not been indicated. The possibility to incorporate material models from CCM into the NOSB-PD formulation is highly advantageous for more realistic simulations of structural behaviors. The aforementioned contributions have motivated the present work in developing a computational framework for the qualitative and quantitative predictions of material damage and failure as well as hyperelastic deformations under prescribed loading conditions. The code is written following an object-oriented design approach.

## 1.4 Research Objectives and Outline

The main purpose of this project is to develop an object-oriented, extensible structural solver for the analysis of elastic deformations under various loading conditions. The code development aims to:

- provide a deeper insight into the NOSB-PD formulation,
- elaborate on all aspects of its numerical implementation,

- highlight the solver's potentials for material modeling and coupling strategies.

This manuscript is organized as follows: Chapter 2 provides a detailed description of the major peridynamic formulations. Chapter 3 elaborates on the material and damage models considered herein. Chapter 4 discusses the different aspects of the numerical implementation, particularly the discretization of equations, the construction of the tangent stiffness matrix and integration schemes. Also, it expounds on elements of the solver design namely the neighbor search and the matrix assembly technique. Finally, Chapter 5 provides an overview of the code and highlights the potential extensions of the current project.

# Chapter 2

# Theoretical Background

## 2.1 Fundamental Concepts

PD is a continuum mechanics theory in which the physical body is subdivided into *material points* of finite volume. As a result, PD is, to some extent, similar to MD. MD deals with discrete entities, i.e., atoms and molecules, at the nano- or microscale. The mutual interactions between these particles are governed by the parameter known as *cutoff radius* $\delta$. In CCM, the state of a point within a body $\mathcal{B}$ is influenced by its *immediate* neighbors only. Therefore, the concept of nonlocality does not arise. In contrast, in PD, each material point within the continuum body $\mathcal{B}$ interacts with its neighbors located within a neighborhood $H_{\boldsymbol{x}}$ delimited by the *horizon* $\delta$.

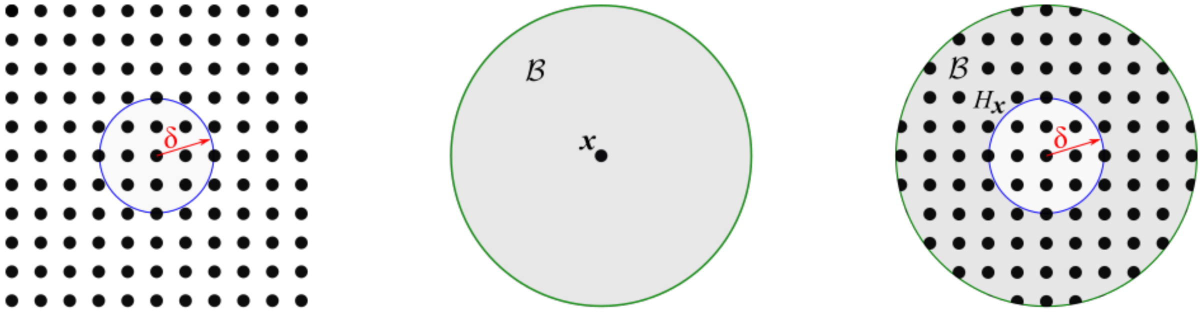

Molecular Dynamics
MD

Classical Continuum Mechanics
CCM

Peridynamics
PD

Figure 2.1: Comparison of MD, CCM and PD.

## 2.2 Governing Equation

### 2.2.1 Bond-based formulation

The peridynamic theory has been introduced in terms of the BB-PD formulation.

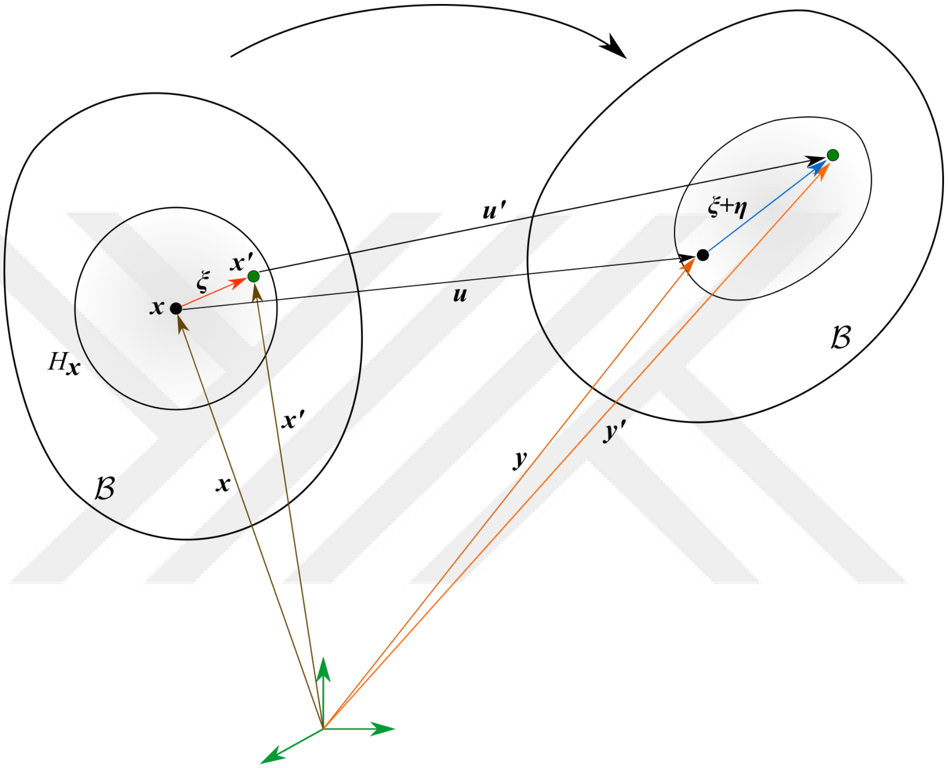

Figure 2.2: Kinematics of a peridynamic continuum.

For material points $\boldsymbol{x}$ and $\boldsymbol{x'}$ in the reference configuration with $\boldsymbol{x'}$ in the neighborhood of $\boldsymbol{x}$, let $\boldsymbol{y}$ and $\boldsymbol{y'}$ denote their respective position vector in the current configuration. Let $\boldsymbol{u}$ and $\boldsymbol{u'}$ denote their respective displacements. The following quantities are defined

$$\boldsymbol{\xi} = \boldsymbol{x'} - \boldsymbol{x}\,, \tag{2.1}$$

$$\boldsymbol{\eta} = \boldsymbol{u'} - \boldsymbol{u}\,, \tag{2.2}$$

$$\boldsymbol{y} = \boldsymbol{x} + \boldsymbol{u}\,, \tag{2.3}$$

$$\boldsymbol{y}' - \boldsymbol{y} = \boldsymbol{\xi} + \boldsymbol{\eta}\,, \tag{2.4}$$

$$s = \frac{|\boldsymbol{\xi} + \boldsymbol{\eta}| - |\boldsymbol{\xi}|}{|\boldsymbol{\xi}|}\,, \tag{2.5}$$

where $\boldsymbol{\xi}$ denotes the relative position vector or bond, $\boldsymbol{\eta}$ the relative displacement vector and

$s$ the *bond stretch*. An alternative representation of the peridynamic formulation has been introduced in [38] based on CCM kinematics.

The governing equation in the BB-PD formulation is

$$\rho\, \ddot{\boldsymbol{u}}(\boldsymbol{x}, t) = \int_{\mathcal{H}} \boldsymbol{f}(\boldsymbol{\eta},\, \boldsymbol{\xi})\, \mathrm{d}V_{\boldsymbol{x}'} + \boldsymbol{b}(\boldsymbol{x}, t)\,, \tag{2.6}$$

where $\rho$ is the density of material point $\boldsymbol{x}$, $\ddot{\boldsymbol{u}}$ its acceleration, $\boldsymbol{f}$ a vector-valued *pairwise force function* of unit $\mathrm{N/m^6}$, $\mathcal{H}$ the neighborhood and $\boldsymbol{b}$ the prescribed body force density of unit $\mathrm{N/m^3}$. The pairwise force function is such that

$$\boldsymbol{f}(-\boldsymbol{\eta},\, -\boldsymbol{\xi}) = -\boldsymbol{f}(\boldsymbol{\eta},\, \boldsymbol{\xi}) \quad \forall \boldsymbol{\eta},\, \boldsymbol{\xi}\,, \tag{2.7}$$

$$(\boldsymbol{\eta} + \boldsymbol{\xi}) \times \boldsymbol{f}(\boldsymbol{\eta},\, \boldsymbol{\xi}) = \boldsymbol{0} \quad \forall \boldsymbol{\eta},\, \boldsymbol{\xi}\,, \tag{2.8}$$

where Eq. (2.7) is a restriction due to the Newton's third law of motion and Eq. (2.8) is the conservation of angular momentum [14].

A *microelastic material* [39] is a material for which there exists a scalar *micropotential function* $w$ such that

$$\boldsymbol{f}(\boldsymbol{\eta},\, \boldsymbol{\xi}) = \frac{\partial w}{\partial \boldsymbol{\eta}}(\boldsymbol{\eta},\, \boldsymbol{\xi}) \tag{2.9}$$

It is indicated that for a microelastic material, the two material points of a bond are "connected by a (possibly nonlinear) spring". Furthermore, the micropotential function $w$ is such that

$$\hat{w}(y,\, \boldsymbol{\xi}) = w(\boldsymbol{\eta},\, \boldsymbol{\xi}) \quad \forall \boldsymbol{\eta},\, \boldsymbol{\xi} \tag{2.10}$$

The pairwise force function in Eq. (2.6) is of the form

$$\boldsymbol{f}(\boldsymbol{\eta},\, \boldsymbol{\xi}) = \frac{\boldsymbol{\xi} + \boldsymbol{\eta}}{|\boldsymbol{\xi} + \boldsymbol{\eta}|}\, f(|\boldsymbol{\xi} + \boldsymbol{\eta}|,\, \boldsymbol{\xi}) \quad \forall \boldsymbol{\eta},\, \boldsymbol{\xi} \tag{2.11}$$

$$f(|\boldsymbol{\xi} + \boldsymbol{\eta}|,\, \boldsymbol{\xi}) = \frac{\partial \hat{w}}{\partial(|\boldsymbol{\xi} + \boldsymbol{\eta}|)}\, (|\boldsymbol{\xi} + \boldsymbol{\eta}|,\, \boldsymbol{\xi}) \quad \forall \boldsymbol{\eta},\, \boldsymbol{\xi} \tag{2.12}$$

Within the context of small deformations, Silling [14] defined the linearization of $\boldsymbol{f}(\boldsymbol{\eta},\, \boldsymbol{\xi})$ as

$$\boldsymbol{f}(\boldsymbol{\eta},\, \boldsymbol{\xi}) = \boldsymbol{C}(\boldsymbol{\xi})\, \boldsymbol{\eta} \quad \forall \boldsymbol{\eta},\, \boldsymbol{\xi}\,, \quad \boldsymbol{C}(\boldsymbol{\xi}) = \frac{\partial \boldsymbol{f}}{\partial \boldsymbol{\eta}}(\boldsymbol{0},\, \boldsymbol{\xi})\,, \tag{2.13}$$

where $\boldsymbol{C}(\boldsymbol{\xi})$ is defined as the *micromodulus tensor*.

The material properties for the BB-PD formulation have been derived by Madenci and Oterkus [3] and will be succinctly presented herein: For the BB-PD formulation, accounting for the pairwise interaction between material points, the force density vector $\boldsymbol{t}$ can be expressed as

$$\boldsymbol{t}(\boldsymbol{\eta},\, \boldsymbol{\xi}, t) = \frac{1}{2}\,\boldsymbol{f}(\boldsymbol{\eta},\, \boldsymbol{\xi}, t) = \frac{1}{2}\,C\,\frac{\boldsymbol{\xi}+\boldsymbol{\eta}}{|\boldsymbol{\xi}+\boldsymbol{\eta}|}\,, \tag{2.14}$$

$$\boldsymbol{t}(-\boldsymbol{\eta},\, -\boldsymbol{\xi}, t) = -\frac{1}{2}\,\boldsymbol{f}(\boldsymbol{\eta},\, \boldsymbol{\xi}, t) = -\frac{1}{2}\,C\,\frac{\boldsymbol{\xi}+\boldsymbol{\eta}}{|\boldsymbol{\xi}+\boldsymbol{\eta}|}\,, \tag{2.15}$$

where $C$ is a parameter dependent on material constants.

Let $\boldsymbol{x}_k$ denote a material point in the reference configuration, $\boldsymbol{x}_j$ a material point in the neighborhood of $\boldsymbol{x}_k$ and $\boldsymbol{t}_{kj}$ the force density vector exerted by $\boldsymbol{x}_j$ on $\boldsymbol{x}_k$. Using Eq. (2.1) through (2.5), the peridynamic strain energy density at $\boldsymbol{x}_k$ is given by

$$\begin{aligned} W_k &= a\,\theta_k^2 - a_2\,\theta_k\,\Delta T_k + a_3\,(\Delta T_k)^2 \\ &\quad + b\sum_{j=1}^{N} w_{kj}\,\left((|\boldsymbol{y}_j - \boldsymbol{y}_k| - |\boldsymbol{x}_j - \boldsymbol{x}_k|) - \alpha\,\Delta T_k\,|\boldsymbol{x}_j - \boldsymbol{x}_k|\right)^2 V_j\,, \end{aligned} \tag{2.16}$$

where $a$, $a_2$, $a_3$, $b$ are material parameters, $\theta_k$ the dilatation, $\alpha$ the thermal expansion coefficient, $V_j$ the volume of material point $\boldsymbol{x}_j$, $N$ the total number of neighbors of $\boldsymbol{x}_k$ and $\Delta T_k$ the temperature change at $\boldsymbol{x}_k$. $w_{kj}$ will be referred to as the *influence function*, a dimensionless parameter in SB-PD.

The dilatation is defined as

$$\theta_k = d\sum_{j=1}^{N} w_{kj}\,(s_{kj} - \alpha\,\Delta T_k)\,\frac{\boldsymbol{y}_j - \boldsymbol{y}_k}{|\boldsymbol{y}_j - \boldsymbol{y}_k|}\cdot(\boldsymbol{x}_j - \boldsymbol{x}_k)\,V_j + 3\,\alpha\,\Delta T_k\,, \tag{2.17}$$

where $d$ is a parameter such that $\theta_k$ is dimensionless and $s_{kj}$ is the stretch of the bond connecting $\boldsymbol{x}_j$ and $\boldsymbol{x}_k$ .

The force density vector $\boldsymbol{t}_{kj}$ is

$$\boldsymbol{t}_{kj} = \frac{1}{V_j}\,\frac{\partial W_k}{\partial(|\boldsymbol{y}_j - \boldsymbol{y}_k|)}\,\frac{\boldsymbol{y}_j - \boldsymbol{y}_k}{|\boldsymbol{y}_j - \boldsymbol{y}_k|} \tag{2.18}$$

Plugging Eq. (2.17) into Eq. (2.16) and using Eq. (2.18), $\boldsymbol{t}_{kj}$ is obtained as

$$\boldsymbol{t}_{kj}\left(\boldsymbol{u}_j - \boldsymbol{u}_k,\, \boldsymbol{x}_j - \boldsymbol{x}_k,\, t\right) = \frac{1}{2}\, A\, \frac{\boldsymbol{y}_j - \boldsymbol{y}_k}{|\boldsymbol{y}_j - \boldsymbol{y}_k|}\,, \tag{2.19}$$

where

$$\begin{aligned} A = 4\, w_{kj} \Big\{ & d\, \frac{\boldsymbol{y}_j - \boldsymbol{y}_k}{|\boldsymbol{y}_j - \boldsymbol{y}_k|} \cdot \frac{\boldsymbol{x}_j - \boldsymbol{x}_k}{|\boldsymbol{x}_j - \boldsymbol{x}_k|}\, (a\, \theta_k - \frac{1}{2} a_2\, \Delta T_k) + b\, ((|\boldsymbol{y}_j - \boldsymbol{y}_k| - |\boldsymbol{x}_j - \boldsymbol{x}_k|) \\ & -\alpha\, \Delta T_k\, |\boldsymbol{x}_j - \boldsymbol{x}_k|) \Big\} \end{aligned} \tag{2.20}$$

Similarly

$$\boldsymbol{t}_{jk}(\boldsymbol{u}_k - \boldsymbol{u}_j,\, \boldsymbol{x}_k - \boldsymbol{x}_j,\, t) = -\frac{1}{2}\, B\, \frac{\boldsymbol{y}_j - \boldsymbol{y}_k}{|\boldsymbol{y}_j - \boldsymbol{y}_k|}\,, \tag{2.21}$$

where

$$\begin{aligned} B = 4\, w_{jk} \Big\{ & d\, \frac{\boldsymbol{y}_k - \boldsymbol{y}_j}{|\boldsymbol{y}_k - \boldsymbol{y}_j|} \cdot \frac{\boldsymbol{x}_k - \boldsymbol{x}_j}{|\boldsymbol{x}_k - \boldsymbol{x}_j|}\, (a\, \theta_j - \frac{1}{2}\, a_2\, \Delta T_j) \\ & + b\, ((|\boldsymbol{y}_k - \boldsymbol{y}_j| - |\boldsymbol{x}_k - \boldsymbol{x}_j|) - \alpha\, \Delta T_j |\boldsymbol{x}_k - \boldsymbol{x}_j|) \Big\} \end{aligned} \tag{2.22}$$

Since $\boldsymbol{t}_{jk}$ and $\boldsymbol{t}_{kj}$ have equal magnitude, $A = B$. Therefore

$$ad = 0 \tag{2.23}$$

As a result

$$C = 4\, b\, w_{kj}\, ((|\boldsymbol{y}_j - \boldsymbol{y}_k| - |\boldsymbol{x}_j - \boldsymbol{x}_k|) - \alpha\, \Delta T_k\, |\boldsymbol{x}_j - \boldsymbol{x}_k|) \tag{2.24}$$

Inserting Eq. (2.24) into Eq. (2.14) yields

$$\boldsymbol{f}(\boldsymbol{u}_j - \boldsymbol{u}_k,\, \boldsymbol{x}_j - \boldsymbol{x}_k, t) = 4\, b\, w_{kj}\, |\boldsymbol{x}_j - \boldsymbol{x}_k|\, (s_{kj} - \alpha\, \Delta T_k)\, \frac{\boldsymbol{y}_j - \boldsymbol{y}_k}{|\boldsymbol{y}_j - \boldsymbol{y}_k|}\,, \tag{2.25}$$

which may be written as

$$\boldsymbol{f}(\boldsymbol{u}_j - \boldsymbol{u}_k,\, \boldsymbol{x}_j - \boldsymbol{x}_k, t) = c\, (s_{kj} - \alpha\, \Delta T_{kj})\, \frac{\boldsymbol{y}_j - \boldsymbol{y}_k}{|\boldsymbol{y}_j - \boldsymbol{y}_k|}\,, \tag{2.26}$$

where $c$ is the *bond constant* [39].

From dimensional analysis on $W_k$, it can be established that

$$\frac{c}{b} = 4\delta \,, \tag{2.27}$$

The constraint arises from the explicit form of the influence function

$$w_{kj} = \frac{\delta}{|\boldsymbol{\xi}|} \tag{2.28}$$

The peridynamic material parameters are determined using simplifying assumptions on the structure's dimensions and by evaluating the strain energy density in Eq. (2.16) from a CCM standpoint. The analysis is carried out considering simple loading cases, specifically *isotropic expansion* and *simple shear*.

| | | | **3D** | **2D** |
|---|---|---|---|---|
| Neighborhood | | | sphere of radius $\delta$ | disk of radius $\delta$, thickness $h$ |
| Coordinate system | | | spherical $(\xi,\, \theta,\, \phi)$ | polar $(\xi,\, \phi)$ |
| Moduli | | | $\kappa = \dfrac{E}{3(1-2\nu)}, \quad \mu = \dfrac{E}{2(1+\nu)}$ | $\kappa = \dfrac{E}{2(1-\nu)}, \quad \mu = \dfrac{E}{2(1+\nu)}$ |
| Constitutive relation ($\boldsymbol{\sigma}_k = \boldsymbol{C}\boldsymbol{\varepsilon}_k$) | | | $\begin{bmatrix} (\sigma_{xx})_k \\ (\sigma_{yy})_k \\ (\sigma_{zz})_k \\ (\sigma_{yz})_k \\ (\sigma_{xz})_k \\ (\sigma_{xy})_k \end{bmatrix} = \begin{bmatrix} \kappa+(4\mu/3) & \kappa-(2\mu/3) & \kappa-(2\mu/3) & 0 & 0 & 0 \\ \kappa-(2\mu/3) & \kappa+(4\mu/3) & \kappa-(2\mu/3) & 0 & 0 & 0 \\ \kappa-(2\mu/3) & \kappa-(2\mu/3) & \kappa+(4\mu/3) & 0 & 0 & 0 \\ 0 & 0 & 0 & \mu & 0 & 0 \\ 0 & 0 & 0 & 0 & \mu & 0 \\ 0 & 0 & 0 & 0 & 0 & \mu \end{bmatrix} \begin{bmatrix} (\varepsilon_{xx})_k \\ (\varepsilon_{yy})_k \\ (\varepsilon_{zz})_k \\ (\gamma_{yz})_k \\ (\gamma_{xz})_k \\ (\gamma_{xy})_k \end{bmatrix}$ | $\begin{bmatrix} (\sigma_{xx})_k \\ (\sigma_{yy})_k \\ (\sigma_{xy})_k \end{bmatrix} = \begin{bmatrix} \kappa+\mu & \kappa-\mu & 0 \\ \kappa-\mu & \kappa+\mu & 0 \\ 0 & 0 & \mu \end{bmatrix} \begin{bmatrix} (\varepsilon_{xx})_k \\ (\varepsilon_{yy})_k \\ (\gamma_{xy})_k \end{bmatrix}$ |
| Parameters evaluation | Isotropic expansion | CCM | $(\varepsilon_{xx})_k = (\varepsilon_{yy})_k = (\varepsilon_{zz})_k = \zeta + \alpha\,\Delta T_k\,, \quad (\gamma_{xy})_k = (\gamma_{xz})_k = (\gamma_{yz})_k = 0$<br>$W_k = \dfrac{9}{2}\,\kappa\,\zeta^2$<br>$\theta_k = \mathrm{tr}(\boldsymbol{\varepsilon}_k) = 3\,(\zeta + \alpha\,\Delta T_k)$ | $(\varepsilon_{xx})_k = (\varepsilon_{yy})_k = \zeta + \alpha\,\Delta T_k\,, \quad (\gamma_{xy})_k = 0$<br>$W_k = 2\,\kappa\,\zeta^2$<br>$\theta_k = 2\,(\zeta + \alpha\,\Delta T_k)$ |
| | | PD | $W_k = a\,\theta_k^2 - a_2\,\theta_k\,\Delta T_k + a_3\,(\Delta T_k)_k^2$<br>$+\, b \int_0^{\delta}\int_0^{2\pi}\int_0^{\pi} \dfrac{\delta}{\xi}\,([\,(1+\zeta+\alpha\,\Delta T_k)\,\xi - \xi] - \alpha\,\Delta T_k\xi)^2\,\xi^2 \sin\phi\,\mathrm{d}\phi\,\mathrm{d}\theta\,\mathrm{d}\xi$<br>$= 3a\,(\zeta+\alpha\,\Delta T_k)^2 - 3a_2\,(\zeta+\alpha\,\Delta T_k)\,\Delta T_k + a_3\,\Delta T_k^2 + \pi b\zeta^2\delta^5$<br>$\theta_k = d \int_0^{\delta}\int_0^{2\pi}\int_0^{\pi} \dfrac{\delta}{\xi}\,([\,(1+\zeta+\alpha\,\Delta T_k)\,\xi - \xi] - \alpha\,\Delta T_k\xi)$<br>$\times \left(\dfrac{\boldsymbol{\xi}}{\xi}\cdot\dfrac{\boldsymbol{\xi}}{\xi}\right)\,\xi^2\,\sin\phi\,\mathrm{d}\phi\,\mathrm{d}\theta\,\mathrm{d}\xi + 3\alpha\,\Delta T_k = \dfrac{4\pi d\delta^4}{3}\zeta + 3\,\alpha\,\Delta T_k$ | $W_k = a\,\theta_k^2 - a_2\,\theta_k\,\Delta T_k + a_3\,(\Delta T_k)_k^2$<br>$+\, bh \int_0^{\delta}\int_0^{2\pi} \dfrac{\delta}{\xi}\,([\,(1+\zeta+\alpha\,\Delta T_k)\,\xi - \xi] - \alpha\,\Delta T_k\xi)^2\,\xi\,\mathrm{d}\theta\,\mathrm{d}\xi$<br>$= 2a\,(\zeta+\alpha\,\Delta T_k)^2 - 2a_2\,(\zeta+\alpha\,\Delta T_k)\,\Delta T_k + a_3\,\Delta T_k^2 + \dfrac{2}{3}\,\pi bh\delta^4\zeta^2$<br>$\theta_k = dh \int_0^{\delta}\int_0^{2\pi} \dfrac{\delta}{\xi}\,([\,(1+\zeta+\alpha\,\Delta T_k)\,\xi - \xi] - \alpha\,\Delta T_k\xi)$<br>$\times \left(\dfrac{\boldsymbol{\xi}}{\xi}\cdot\dfrac{\boldsymbol{\xi}}{\xi}\right)\,\xi\,\mathrm{d}\theta\,\mathrm{d}\xi + 2\,\alpha\,\Delta T_k = \pi dh\delta^3\zeta + 2\,\alpha\,\Delta T_k$ |
| | Simple shear | CCM | $(\gamma_{xy})_k = \zeta, \quad (\varepsilon_{xx})_k \;= (\varepsilon_{yy})_k = (\varepsilon_{zz})_k = (\gamma_{xz})_k = (\gamma_{yz})_k = \Delta T_k = 0$<br>$W_k = \dfrac{1}{2}\,\mu\,\zeta^2$<br>$\theta_k = 0$ | $(\gamma_{xy})_k = \zeta, \quad (\varepsilon_{xx})_k \;= (\varepsilon_{yy})_k = \Delta T_k = 0$<br>$W_k = \dfrac{1}{2}\,\mu\,\zeta^2$<br>$\theta_k = 0$ |
| | | PD | $W_k = b \int_0^{\delta}\int_0^{2\pi}\int_0^{\pi} \dfrac{\delta}{\xi}\,\left(\left[1 + \dfrac{\zeta\sin(2\phi)\sin(\theta)}{2}\right]\,\xi - \xi\right)^2\,\xi^2\sin\phi\,\mathrm{d}\phi\,\mathrm{d}\theta\,\mathrm{d}\xi = \dfrac{b\pi\delta^5\zeta^2}{15}$ | $W_k = bh \int_0^{\delta}\int_0^{2\pi} \dfrac{\delta}{\xi}\,([1 + (\sin(\theta)\,\cos(\theta))\zeta]\,\xi - \xi)^2\,\xi\,\mathrm{d}\theta\,\mathrm{d}\xi = \dfrac{\pi h\delta^4\zeta^2}{12}b$ |
| Peridynamic parameters | | | Isotropic expansion: $(W_k)_{CCM} = (W_k)_{PD} \Rightarrow \begin{cases} 9a + \pi b\delta^5 = \dfrac{9}{2}\,\kappa \\ a_2 = 6\alpha a \\ a_3 = 9\alpha^2 a \end{cases}$<br>Isotropic expansion: $(\theta_k)_{CCM} = (\theta_k)_{PD} \Rightarrow d = \dfrac{9}{4\pi\delta^4}$<br>Simple shear: $(W_k)_{CCM} = (W_k)_{PD} \Rightarrow b = \dfrac{15\mu}{2\pi\delta^5}$<br>Eq. (2.23) and Eq. (2.27) $\Rightarrow \kappa = \dfrac{5\mu}{3}\,, \quad \nu = \dfrac{1}{4}\,, \quad c = \dfrac{18\kappa}{\pi\delta^4}$ | Isotropic expansion: $(W_k)_{CCM} = (W_k)_{PD} \Rightarrow \begin{cases} 4a + \dfrac{2}{3}\pi bh\delta^4 = 2\,\kappa \\ a_2 = 4\alpha a \\ a_3 = 4\alpha^2 a \end{cases}$<br>Isotropic expansion: $(\theta_k)_{CCM} = (\theta_k)_{PD} \Rightarrow d = \dfrac{2}{\pi h\delta^3}$<br>Simple shear : $(W_k)_{CCM} = (W_k)_{PD} \Rightarrow b = \dfrac{6\mu}{\pi h\delta^4}$<br>Eq. (2.23) and Eq. (2.27) $\Rightarrow \kappa = 2\mu\,, \quad \nu = \dfrac{1}{3}\,, \quad c = \dfrac{12\kappa}{\pi h\delta^3}$ |

Table 2.1: Material parameters evaluation in BB-PD.

Additionally, derivations of the BB-PD bond constants for plane stress and plane strain conditions have been presented in [40].

Thus, the traditional BB-PD model has several drawbacks in terms of modeling capabilities due to the constraints on material parameters. Silling and Askari [39] introduced a failure criterion at the bond level such that, beyond a specified limit referred to as the *critical stretch*, the bond is permanently broken. This variant of the BB-PD model is known as the *prototype microelastic brittle* (PMB) model.

Various attempts have been made to extend the BB-PD model. As observed by Han et al. [41], overcoming the limitation on the Poisson's ratio [42] has been a major research focus. Furthermore, improved models account for particle rotations and shear deformations for beams, bending of plates [43] as well as material anisotropy [44].

Despite its success in different types of problems, many challenges are still present. Notably, the improved models are tailored to specific problems. Also, more advanced constitutive models that can capture geometrically nonlinear deformations need to be developed.

### 2.2.2 State-based formulation

The state-based formulation was then proposed as a remedy to the limitations of BB-PD. Specifically, the two forms of the state-based formulation relax the assumption of pairwise interactions between material points: In the OSB-PD, the forces act in opposite directions but have different magnitude. In the NOSB-PD, the forces between the material points can act in arbitrary directions.

Central to the SB-PD theory is the concept of *states*. These objects are defined as mappings of a vector $\boldsymbol{\xi}$ to a tensor of order $m$, $m \in \mathbb{Z}$ and $m \geqslant 0$. The mathematical properties of states are thoroughly described in [15].

The following quantities are defined

$$\underline{\boldsymbol{X}}\langle\boldsymbol{\xi}\rangle = \boldsymbol{\xi}\,, \tag{2.29}$$

$$\underline{\boldsymbol{Y}}\langle\boldsymbol{\xi}\rangle = \boldsymbol{y}' - \boldsymbol{y} = (\boldsymbol{x}' + \boldsymbol{u}') - (\boldsymbol{x} + \boldsymbol{u}) = \boldsymbol{\xi} + \boldsymbol{\eta}\,, \tag{2.30}$$

where $\underline{\boldsymbol{X}}\langle\boldsymbol{\xi}\rangle$ is referred to as the initial deformation state and $\underline{\boldsymbol{Y}}\langle\boldsymbol{\xi}\rangle$ the current deformation state.

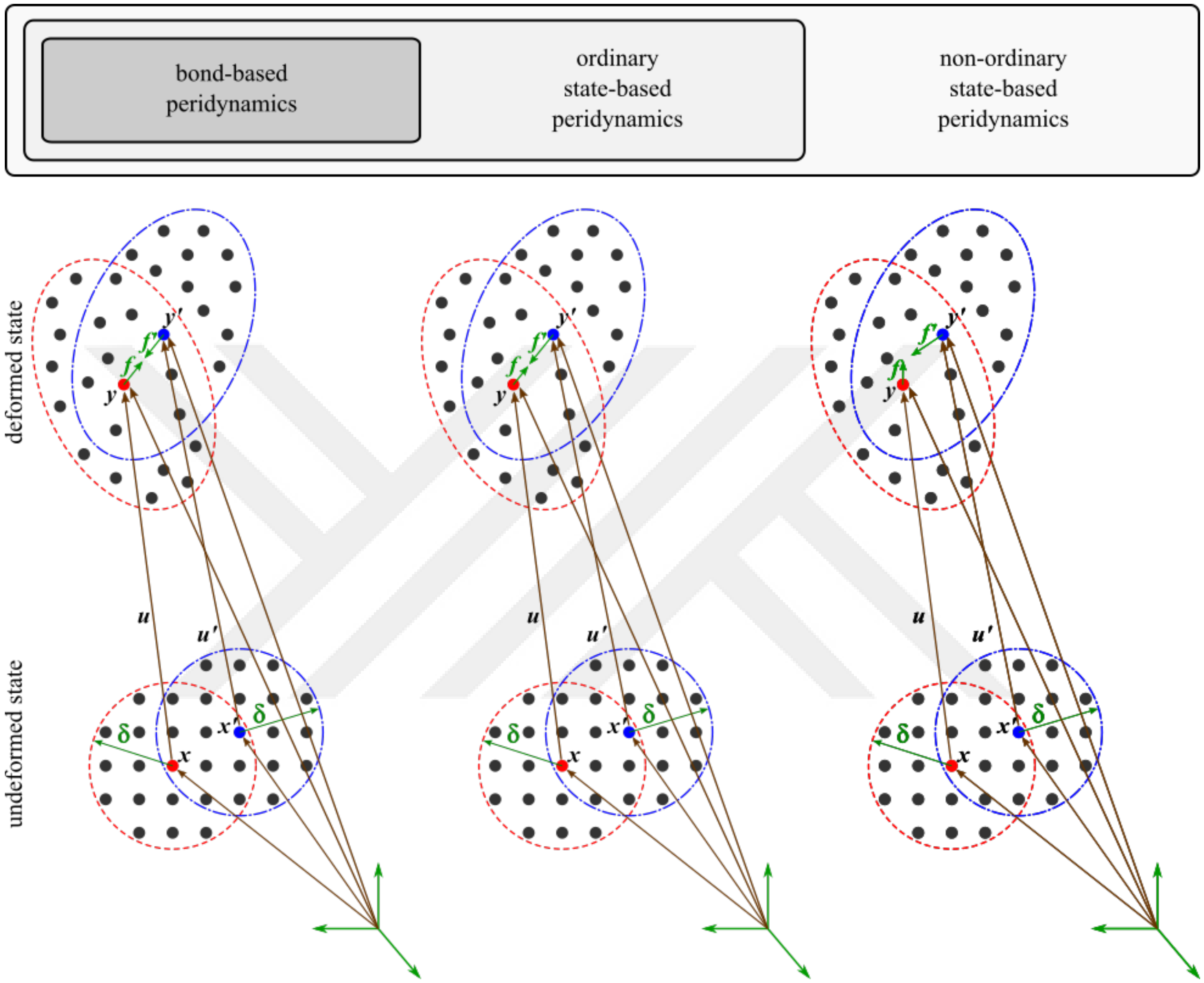

Figure 2.3: Illustration of the BB-PD, OSB-PD and NOSB-PD formulations.

The governing equation of the NOSB-PD is expressed as

$$\rho\,\ddot{\boldsymbol{u}}(\boldsymbol{x},t)=\int_{\mathcal{H}}\{\underline{\boldsymbol{T}}[\boldsymbol{x},t]\langle\boldsymbol{\xi}\rangle-\underline{\boldsymbol{T}}[\boldsymbol{x}',t]\langle-\boldsymbol{\xi}\rangle\}\,\mathrm{d}V_{\boldsymbol{x}'}+\boldsymbol{b}(\boldsymbol{x},t)\,, \tag{2.31}$$

where $\underline{\boldsymbol{T}}$ denotes the force state.

The *linear peridynamic solid* (LPS) [39] is one of the main constitutive models in the OSB-PD theory. A material is said to be *ordinary* if there exist a scalar force state $\underline{t}$ and a vector state $\underline{\boldsymbol{M}}$ such that

$$\underline{\boldsymbol{T}}=\underline{t}\,\underline{\boldsymbol{M}}\,, \tag{2.32}$$

where $\underline{\boldsymbol{M}}\langle\boldsymbol{\xi}\rangle = \dfrac{\boldsymbol{\xi}+\boldsymbol{\eta}}{|\boldsymbol{\xi}+\boldsymbol{\eta}|}$.

The force scalar state is given by

$$\underline{t} = \frac{3\,\kappa\,\theta}{m}\underline{\omega}\,|\boldsymbol{\xi}| + \frac{15\,\mu}{m}\,\underline{\omega}\,\underline{e}^{d}\,, \tag{2.33}$$

where $\underline{\omega}$ is a spherical influence function and $\underline{e}$ denotes the extension scalar state given by

$$\underline{e}[\boldsymbol{x},t]\langle\boldsymbol{\xi}\rangle = |\boldsymbol{\xi}+\boldsymbol{\eta}| - |\boldsymbol{\xi}|\,, \tag{2.34}$$

The isotropic and deviatoric parts of $\underline{e}$ are respectively

$$\underline{e}^{i} = \frac{\theta\,|\boldsymbol{\xi}|}{3}, \quad \underline{e}^{d} = \underline{e} - \underline{e}^{i}. \tag{2.35}$$

$m$ is referred to as the *weighted volume* and is defined as

$$m[\boldsymbol{x}] = \int_{\mathcal{H}} \underline{\omega}\,(|\boldsymbol{\xi}|)^2\,\mathrm{d}V_{\boldsymbol{\xi}} \tag{2.36}$$

$\theta$ is the dilatation defined as

$$\theta[\boldsymbol{x},t] = \frac{3}{m[\boldsymbol{x}]}\int_{\mathcal{H}} \underline{\omega}\,|\boldsymbol{\xi}|\,\underline{e}[\boldsymbol{x},t]\langle\boldsymbol{\xi}\rangle\,\mathrm{d}V_{\boldsymbol{\xi}} \tag{2.37}$$

Seleson et al. [45] have shown that, for $\nu = 1/4$, the LPS model recovers the PMB model with

$$\mu = \frac{3}{5}\,\kappa\,, \tag{2.38}$$

$$\underline{t}[\boldsymbol{x},t]\,\langle\boldsymbol{\xi}\rangle = \frac{1}{2}\left(\frac{18\,\kappa}{\pi\,\delta^4}\right)\,s \tag{2.39}$$

The main differences between the NOSB-PD and the CCM formulations are the definitions of the balance laws. The term div$\boldsymbol{\sigma}$ is replaced by the integral operator in the NOSB-PD, which permits a discontinuous displacement field (Table 2.2).

| **Balance law** | **PD** | **CCM** |
|---|---|---|
| Linear momentum balance | $\rho\,\ddot{\boldsymbol{u}}(\boldsymbol{x},t) = \int_{\mathcal{H}} \{\underline{\boldsymbol{T}}[\boldsymbol{x},t]\langle\boldsymbol{\xi}\rangle - \underline{\boldsymbol{T}}[\boldsymbol{x'},t]\langle-\boldsymbol{\xi}\rangle\}\,\mathrm{d}V_{\boldsymbol{x'}} + \boldsymbol{b}(\boldsymbol{x},t)$ | $\rho\,\ddot{\boldsymbol{u}}(\boldsymbol{x},t) = \mathrm{div}\boldsymbol{\sigma} + \boldsymbol{b}(\boldsymbol{x},t)$ |
| Angular momentum balance | $\int_{\mathcal{H}} \underline{\boldsymbol{Y}}\langle\boldsymbol{\xi}\rangle \times \underline{\boldsymbol{T}}\langle\boldsymbol{\xi}\rangle\,\mathrm{d}V_{\boldsymbol{\xi}} = \boldsymbol{0}$ | $\boldsymbol{\sigma} = \boldsymbol{\sigma}^T$ |

Table 2.2: Comparison of balance laws between PD and CCM.

The force state $\underline{\boldsymbol{T}}\langle\boldsymbol{\xi}\rangle$ acts on a bond $\boldsymbol{\xi}$ and is expressed as

$$\underline{\boldsymbol{T}}\langle\boldsymbol{\xi}\rangle = \omega(|\boldsymbol{\xi}|)\boldsymbol{P}\boldsymbol{K}^{-1}\boldsymbol{\xi}\,, \tag{2.40}$$

where $\omega(|\boldsymbol{\xi}|)$ is referred to as the *influence function*, $\boldsymbol{P}$ the Piola stress tensor and $\boldsymbol{K}$ the shape tensor defined as

$$\boldsymbol{K} = \int_{\mathcal{H}} \omega(|\boldsymbol{\xi}|)\,((\boldsymbol{x'} - \boldsymbol{x}) \otimes (\boldsymbol{x'} - \boldsymbol{x}))\,\mathrm{d}V'\,, \tag{2.41}$$

where the symbol $\otimes$ indicates the dyadic product of two vectors.

It is worth noting that the balance laws in the state-based theory are satisfied *over a bounded body $\mathcal{B}$*.

The shape tensor $\boldsymbol{K}$ acts as a volume-averaging quantity and was shown to be a function of the horizon volume and size [3]. It is worth mentioning that the shape tensor $\boldsymbol{K}$ is symmetric positive definite.

An interesting concept is that of the *correspondence material model*: for a given CCM elastic material model, the peridynamic constitutive model yields the same physical properties under *affine deformations* through the nonlocal deformation gradient tensor $\boldsymbol{F}$. In the NOSB-PD, the *approximate nonlocal deformation gradient tensor* is

$$\boldsymbol{F} = \left[\int_{\mathcal{H}} \omega(|\boldsymbol{\xi}|)\,((\boldsymbol{y'} - \boldsymbol{y}) \otimes (\boldsymbol{x'} - \boldsymbol{x}))\,\mathrm{d}V'\right]\boldsymbol{K}^{-1} \tag{2.42}$$

In the context of the correspondence material model, $\boldsymbol{P} = \boldsymbol{P}(\boldsymbol{F})$ is obtained using a constitutive model from CCM.

## 2.3 Influence Function

The influence function $\omega$ is a scalar state that is crucial in SB-PD. It acts as a weight parameter on the contribution of the individual bonds within $\mathcal{H}$ to the computation of related quantities. Specifically, bond termination can be achieved by means of the influence function in fracture simulations. A non-negative scalar state $\omega$ is referred to as *spherical* if it is solely a function of $|\boldsymbol{\xi}|$ [15]. The proper choice of the influence function remains an open question in PD. In this case, a Gaussian influence function is chosen

$$\omega\langle\boldsymbol{\xi}\rangle = e^{-|\boldsymbol{\xi}|^2/\delta^2} \tag{2.43}$$

## 2.4 Zero-Energy Modes Control

Despite its convenience for modeling material behaviors, the peridynamic correspondence model, in its original form, is inherently affected by *zero-energy mode instability.* Silling [46] recently showed that the latter emerges due to *material instability.* By means of an energy minimization approach, he demonstrated that, in the correspondence material models, multiple deformations of a neighborhood can be associated with the same $\boldsymbol{F}$ for a radially symmetric influence function. In other words, the zero-energy modes stem from the erroneous computation of the approximate deformation gradient tensor.

For a practical understanding of their origin, the explanation of Breitenfeld [47] will be reported herein:

Within a neighborhood $\mathcal{H}$ of radius $\delta$, let the material point $\boldsymbol{x}$ be displaced by a small perturbation while its neighbors are fixed. Thus, the new deformation state is

$$\underline{\boldsymbol{Y}}'\langle\boldsymbol{\xi}\rangle = \underline{\boldsymbol{Y}}\langle\boldsymbol{\xi}\rangle - \boldsymbol{u}' \tag{2.44}$$

The new deformation gradient is

$$\boldsymbol{F}' = \boldsymbol{F} - \boldsymbol{u}' \otimes \left( \int_{\mathcal{H}} \omega(|\boldsymbol{\xi}|)\, \boldsymbol{\xi}\, \mathrm{d}V_{\boldsymbol{x}'} \right) \boldsymbol{K}^{-1} = \boldsymbol{F} \tag{2.45}$$

since the integral is evaluated inside a sphere in a within a three-dimensional context. Breitenfeld noted that the existence of zero-energy modes in the correspondence models are “due to the weak coupling of each point to its own family".

In a meshless discretization, the manifest effects of zero-energy modes are oscillations in the displacement, stress and strain fields, that is, *numerical instabilities*. Therefore, they must be completely suppressed or at least mitigated since they induce incorrect results.

Various methods have been developed to control the effects of zero-energy modes. Notably, Breitenfeld [47] and Silling [46] proposed the addition of a supplemental force state to Eq. (2.40). Although these techniques reduce the zero-energy modes, they require a parameter adjustment which may cause practical issues; for instance, the supplemental forces could dominate the total force state term if the coefficients were chosen to be large. Yaghoobi et al. [48] proposed a technique based on higher-order approximations of the nonlocal deformation gradient tensor to control the zero-energy modes. Following the approach presented in [46], Li et al. [49] introduced a stabilized NOSB-PD formulation free of parameter adjustment; the supplemental force state is derived according to an energy-based approach. It is also noted that in a recent contribution, Gu et al. [50] presented an alternative formulation of the NOSB-PD internal force density vector.

In this project, the supplemented force state described in [49] is used for simplicity. The zero-energy modes control technique is based on the *non-uniform deformation state* $\boldsymbol{z}\langle\boldsymbol{\xi}\rangle$ defined as

$$\boldsymbol{z}\langle\boldsymbol{\xi}\rangle = \underline{\boldsymbol{Y}}\langle\boldsymbol{\xi}\rangle - \boldsymbol{F}\boldsymbol{\xi} \tag{2.46}$$

In the Prototype Microelastic Brittle (PMB) material model, a variant of the BB-PD formulation, the *micromodulus tensor* is given by

$$\boldsymbol{C}(\boldsymbol{\xi}) = c\,\boldsymbol{\xi} \otimes \boldsymbol{\xi}/|\boldsymbol{\xi}|^3\,, \tag{2.47}$$

where $c$ is the *bond constant*

$$c = 18\kappa/\pi\delta^4\,, \tag{2.48}$$

where $\kappa$ denotes the bulk modulus

$$\kappa = E/(3(1-2\nu)) \tag{2.49}$$

The stabilizing term is defined as

$$\underline{\boldsymbol{T}}_s\langle\boldsymbol{\xi}\rangle = \frac{1}{2}\,\omega(|\boldsymbol{\xi}|)\,\boldsymbol{C}\,\boldsymbol{z}\langle\boldsymbol{\xi}\rangle \tag{2.50}$$

Using Eq. (2.40) and (2.50), the total force state is therefore

$$\underline{\boldsymbol{T}}\langle\boldsymbol{\xi}\rangle = \omega(|\boldsymbol{\xi}|)\boldsymbol{P}\boldsymbol{K}^{-1}\boldsymbol{\xi} + \frac{1}{2}\,\omega(|\boldsymbol{\xi}|)\,\boldsymbol{C}\,\boldsymbol{z}\langle\boldsymbol{\xi}\rangle \tag{2.51}$$

## 2.5 Boundary Conditions

The enforcement of boundary conditions (BCs) in PD is drastically different from that of other numerical methods based on CCM such as the FEM: As explained by Silling [14], natural boundary conditions do not appear when deriving the Euler-Lagrange equations from the potential energy functional. Moreover, no traction forces in the CCM sense are present.

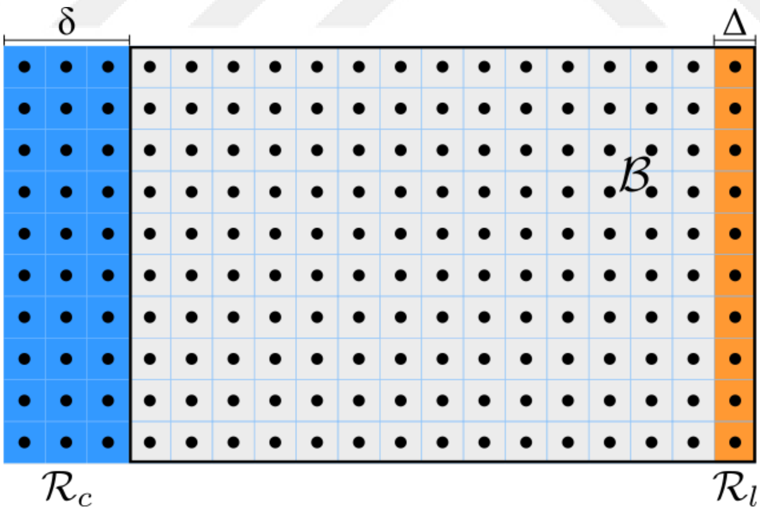

Figure 2.4: Application of boundary conditions in PD.

In the above figure, DBCs including displacements and velocities are applied to all the material points in $\mathcal{R}_c$ which will be reflected to the material points within the body $\mathcal{B}$. Regarding tractions and other external forces, they cannot be directly applied to a peridynamic continuum but must be expressed as force densities enforced through a material layer $\mathcal{R}_l$ near the domain boundary [14, 3].

## 2.6 Correction Procedures

### 2.6.1 Volume correction

In order to improve the accuracy of the solutions, a volume correction procedure is applied to the material points lying on the horizon [3] by implementing *partial volume algorithms.* Let $\Delta$ denote the spacing between material points in a uniform grid and $r = \Delta/2$.

As proposed by Hu, Ha and Bobaru [51], an *improved algorithm* to compute the volume correction factor is as follows

$$v_c = \begin{cases} 1 & \text{if} \quad l < \delta - r\,, \\ \dfrac{\delta + r - l}{2r} & \text{if} \quad l \leq \delta + r\,, \\ 0 & \text{otherwise}\,, \end{cases} \tag{2.52}$$

where $l = |\boldsymbol{\xi}|$.

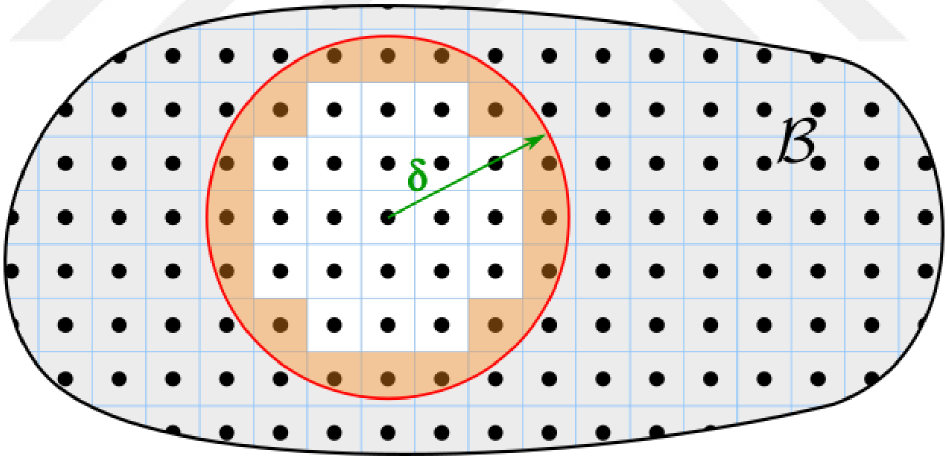

Figure 2.5: Illustration of full and partial volumes within a neighborhood.

In Fig. (2.5), the material points in white have full volumes whereas the ones in orange have partial volumes since they are located at the limit of the neighborhood.

### 2.6.2 Surface correction

In the BB-PD and OSB-PD formulations, the material models are derived assuming that the material points located in the bulk, i.e., having a full neighborhood. This assumption is no longer valid in the vicinity of free surfaces and/or material interfaces, where material points have incomplete neighborhoods due to truncated horizons. This phenomenon affects the accuracy of the solution as it alters the material properties in these regions. As a result, corrective procedures are required.

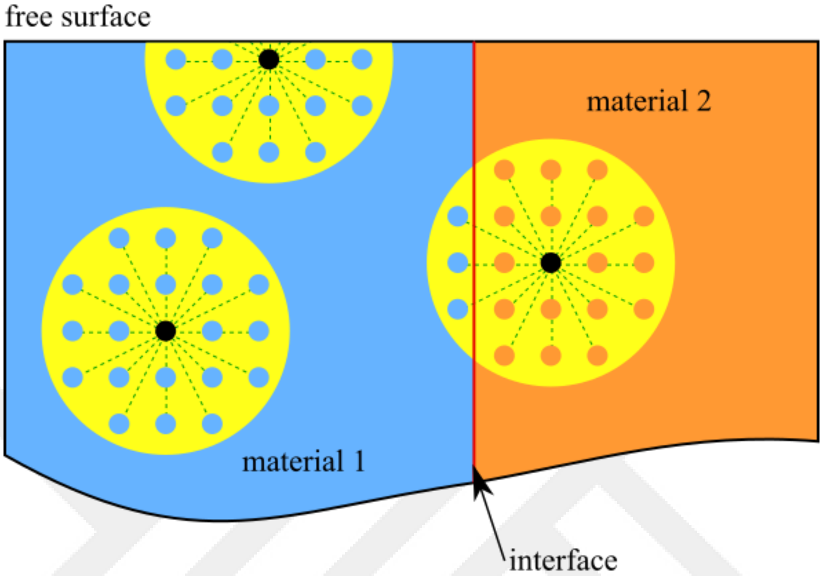

Figure 2.6: Material points' neighborhoods near free surfaces and interfaces.

Fig. (2.6) depicts the states of neighborhoods within the bulk; near the domain boundary, where the neighborhood is incomplete and across material interfaces, at which a neighborhood consists of material points of different properties. For the BB-PD and OSB-PD formulations, given that the values of the parameters $b$ and $d$ in Eqs. (2.16) and (2.17) are dependent on the integration domain, i.e., the neighborhood, corrective procedures are required. To address these *surface effects*, various techniques have been developed to compute surface correction factors [52, 3]. According to the technique described in [3], surface correction factors are obtained by computing the ratio of the CCM strain energy density with the PD strain energy density assuming simple loading cases in each spatial direction. Such a procedure is not required in the context of the NOSB-PD formulation. For a correspondence material model, the evaluation of $\boldsymbol{F}$ need not be over a full neighborhood.

# Chapter 3

# Material and Damage Models

## 3.1 Constitutive Model

The state-based formulation of PD allows the generalization of the initial bond-based model by accounting for volumetric changes and rotations [15]. It is shown that Eq. (2.31) satisfies the linear momentum balance for any bounded body $\mathcal{B}$, regardless of the evaluation of $\underline{\boldsymbol{T}}$. Indeed, rearranging Eq. (2.31)and integrating over the body $\mathcal{B}$ gives

$$\int_{\mathcal{B}} (\rho\, \ddot{\boldsymbol{u}}(\boldsymbol{x},t) - \boldsymbol{b}(\boldsymbol{x},t))\, \mathrm{d}V_{\boldsymbol{x}} = \int_{\mathcal{H}} \{\underline{\boldsymbol{T}}[\boldsymbol{x},t]\langle\boldsymbol{\xi}\rangle - \underline{\boldsymbol{T}}[\boldsymbol{x}',t]\langle-\boldsymbol{\xi}\rangle\}\, \mathrm{d}V_{\boldsymbol{x}'}\, \mathrm{d}V_{\boldsymbol{x}} \tag{3.1}$$

Given that $\underline{\boldsymbol{T}}[\boldsymbol{x},t] = \boldsymbol{0}$ when $\boldsymbol{x}' \notin \mathcal{H}_{\boldsymbol{x}}$, changing the domain of integration from $\mathcal{H}_{\boldsymbol{x}}$ to $\mathcal{B}$ and applying change of variables such that $\boldsymbol{x}' = \boldsymbol{x}$, Eq. (3.1) becomes

$$\int_{\mathcal{B}} (\rho\, \ddot{\boldsymbol{u}}(\boldsymbol{x},t) - \boldsymbol{b}(\boldsymbol{x},t))\, \mathrm{d}V_{\boldsymbol{x}} = \int_{\mathcal{B}} \int_{\mathcal{B}} \{\underline{\boldsymbol{T}}[\boldsymbol{x},t]\langle\boldsymbol{\xi}\rangle - \underline{\boldsymbol{T}}[\boldsymbol{x},t]\langle\boldsymbol{\xi}\rangle\}\, \mathrm{d}V_{\boldsymbol{x}'}\, \mathrm{d}V_{\boldsymbol{x}} = \boldsymbol{0} \tag{3.2}$$

According to [15], for any deformation of $\mathcal{B}$ associated with the constitutive model defined by $\underline{\boldsymbol{T}}$, the angular momentum balance holds

$$\int_{\mathcal{B}} \boldsymbol{y}(\boldsymbol{x},t) \times (\rho\, \ddot{\boldsymbol{u}}(\boldsymbol{x},t) - \boldsymbol{b}(\boldsymbol{x},t))\, \mathrm{d}V_{\boldsymbol{x}} = \boldsymbol{0} \tag{3.3}$$

The constitutive model is such that

$$\int_{\mathcal{H}} \underline{\boldsymbol{Y}}\langle\boldsymbol{\xi}\rangle \times \underline{\boldsymbol{T}}\langle\boldsymbol{\xi}\rangle \,\mathrm{d}V_{\boldsymbol{\xi}} = \boldsymbol{0} \quad \forall \underline{\boldsymbol{Y}} \in \mathcal{V} \tag{3.4}$$

It is noted that $\underline{\boldsymbol{T}}$ is assumed to be bounded and Riemann-integrable on $\mathcal{H}$.

Indeed, using Eqs. (2.1) through (2.4), (2.30), (2.31),

$$\begin{aligned}
\int_{\mathcal{B}} \boldsymbol{y} \times (\rho\,\ddot{\boldsymbol{u}} - \boldsymbol{b})\,\mathrm{d}V_{\boldsymbol{x}} &= \int_{\mathcal{B}} (\boldsymbol{x} + \boldsymbol{u}) \times (\rho\,\ddot{\boldsymbol{u}} - \boldsymbol{b})\,\mathrm{d}V_{\boldsymbol{x}} \\
&= \int_{\mathcal{B}}\int_{\mathcal{B}} (\boldsymbol{x} + \boldsymbol{u}) \times (\underline{\boldsymbol{T}}[\boldsymbol{x}, t]\langle\boldsymbol{\xi}\rangle - \underline{\boldsymbol{T}}[\boldsymbol{x}', t]\langle-\boldsymbol{\xi}\rangle)\,\mathrm{d}V_{\boldsymbol{x}'}\,\mathrm{d}V_{\boldsymbol{x}} \\
&= \int_{\mathcal{B}}\int_{\mathcal{B}} (\boldsymbol{x} + \boldsymbol{u}) \times \underline{\boldsymbol{T}}[\boldsymbol{x}, t]\langle\boldsymbol{\xi}\rangle\,\mathrm{d}V_{\boldsymbol{x}'}\,\mathrm{d}V_{\boldsymbol{x}} \\
&- \int_{\mathcal{B}}\int_{\mathcal{B}} (\boldsymbol{x} + \boldsymbol{u}) \times \underline{\boldsymbol{T}}[\boldsymbol{x}', t]\langle-\boldsymbol{\xi}\rangle\,\mathrm{d}V_{\boldsymbol{x}'}\,\mathrm{d}V_{\boldsymbol{x}} \\
&= \int_{\mathcal{B}}\int_{\mathcal{B}} (\boldsymbol{x} + \boldsymbol{u}) \times \underline{\boldsymbol{T}}[\boldsymbol{x}, t]\langle\boldsymbol{\xi}\rangle\,\mathrm{d}V_{\boldsymbol{x}'}\,\mathrm{d}V_{\boldsymbol{x}} \\
&- \int_{\mathcal{B}}\int_{\mathcal{B}} (\boldsymbol{x}' + \boldsymbol{u}') \times \underline{\boldsymbol{T}}[\boldsymbol{x}, t]\langle\boldsymbol{\xi}\rangle\,\mathrm{d}V_{\boldsymbol{x}}\,\mathrm{d}V_{\boldsymbol{x}'} \text{ (variable change)} \\
&= -\int_{\mathcal{B}}\int_{\mathcal{B}} ((\boldsymbol{x}' + \boldsymbol{u}') - (\boldsymbol{x} + \boldsymbol{u})) \times \underline{\boldsymbol{T}}[\boldsymbol{x}, t]\langle\boldsymbol{\xi}\rangle\,\mathrm{d}V_{\boldsymbol{x}'}\,\mathrm{d}V_{\boldsymbol{x}} \\
&= -\int_{\mathcal{B}}\int_{\mathcal{B}} ((\boldsymbol{y}' - \boldsymbol{y}) \times \underline{\boldsymbol{T}}[\boldsymbol{x}, t]\langle\boldsymbol{\xi}\rangle\,\mathrm{d}V_{\boldsymbol{x}'}\,\mathrm{d}V_{\boldsymbol{x}} \\
&= -\int_{\mathcal{B}}\int_{\mathcal{H}} \underline{\boldsymbol{Y}}\langle\boldsymbol{\xi}\rangle \times \underline{\boldsymbol{T}}\langle\boldsymbol{\xi}\rangle\,\mathrm{d}V_{\boldsymbol{\xi}}\,\mathrm{d}V_{\boldsymbol{x}} = \boldsymbol{0}
\end{aligned}$$

For practical applications, it is desired that the peridynamic material response is analogous to that of a CCM material model. The NOSB-PD formulation allows the incorporation of a material model from CCM into the constitutive relation to evaluate the force state. Through the deformation gradient tensor $\boldsymbol{F}$ based on the deformation state $\underline{\boldsymbol{Y}}$, the following *correspondence* may be established, within the context of homogeneous deformations

$$\Omega(\underline{\boldsymbol{Y}}) = W(\boldsymbol{F}(\underline{\boldsymbol{Y}}))\,, \tag{3.5}$$

where $\Omega$ denotes the strain energy density of the peridynamic material model and $W$ that of the CCM material model. Numerous studies dealing with quasistatics in NOSB-PD employ a linear elastic material model.

In this work, it is desired to investigate the behavior of structures undergoing large deformations. In order to account for geometric nonlinearity, hyperelastic material models are considered. For such materials, the constitutive relation derives from a strain energy density (SED) function. In particular, the Neo-Hookean material model is employed. The following SED function is considered

$$W = \frac{1}{2}\,\lambda\,(\ln J)^2 + \frac{1}{2}\,\mu\,(\boldsymbol{F} : \boldsymbol{F} - 3 - 2\ln J)\,, \tag{3.6}$$

where $J = \det(\boldsymbol{F})$ denotes the determinant of $\boldsymbol{F}$, $\lambda$ and $\mu$ the Lamé parameters.

From Eq. (3.6), the Piola stress tensor is obtained as

$$\boldsymbol{P} = \frac{\partial W}{\partial \boldsymbol{F}} = \lambda\,\ln J\,\boldsymbol{F}^{\text{-T}} + \mu\,(\boldsymbol{F} - \boldsymbol{F}^{\text{-T}}) \tag{3.7}$$

## 3.2 Damage Models

Owing to its formulation and meshfree discretization, the peridynamic theory has been successfully used to analyze crack initiation and propagation under various loading conditions [22, 18]. A major feature of PD is that damage initiation and propagation are achieved through *irreversible bond rupture*, the latter is governed by a pre-defined damage criterion. In the case of pre-cracked bodies, the analysis is carried out such that, prior to the integration, all bonds passing through crack surfaces are permanently terminated.

Several criteria are available including the critical stretch, the equivalent and averaged volumetric strain failure criteria [20], the energy-based criterion [53] and the cumulative damage model for rate-dependent constitutive models [22, 23].

Within the context of quasi-static analysis, the damage criteria are associated with the critical energy release rate $G_c$, i.e. based on the Griffith theory. The critical stretch $s_c$ has originally been derived within the BB-PD theory [39] and is expressed as

$$s_c = \sqrt{\frac{5\,G_c}{9\,\kappa\,\delta}} \tag{3.8}$$

For state-based material models [3], the critical stretch is

$$s_c = \begin{cases} \sqrt{\dfrac{G_c}{\left(\dfrac{6}{\pi}\mu + \dfrac{16}{9\pi^2}(\kappa - 2\mu)\right)\delta}} & \text{in 2D}\,, \\ \sqrt{\dfrac{G_c}{\left(3\mu + \left(\dfrac{3}{4}\right)^4\left(\kappa - \dfrac{5}{3}\mu\right)\right)\delta}} & \text{in 3D} \end{cases} \tag{3.9}$$

At every time step, the deformation of a bond is monitored and compared to $s_c$ by means of a history-dependent, scalar-valued function $\mu$ such that

$$\mu(\boldsymbol{\xi}, t) = \begin{cases} 1 & \text{if} \quad s < s_c \quad \forall t > 0\,, \\ 0 & \text{otherwise} \end{cases} \tag{3.10}$$

The damage state of a material point is quantified by a quantity referred to as the *local damage index* given by

$$\varphi(\boldsymbol{x}, t) = 1 - \frac{\displaystyle\int_{\mathcal{H}} \mu(\boldsymbol{\xi}, t)\,\mathrm{d}V'}{\displaystyle\int_{\mathcal{H}} \mathrm{d}V'}\,, \quad 0 \leqslant \varphi(\boldsymbol{x}, t) \leqslant 1 \tag{3.11}$$

A local damage index of 1 means that all the bonds associated with the material point are broken.

The energy-based damage criterion [53] is such that

$$\mu(\boldsymbol{\xi}, t) = \begin{cases} 1 & \text{if} \quad w_{\boldsymbol{\xi}} < w_c \quad \forall t > 0\,, \\ 0 & \text{otherwise}\,, \end{cases} \tag{3.12}$$

where $w_{\boldsymbol{\xi}} = (\underline{\boldsymbol{T}}[\boldsymbol{x}, t]\langle\boldsymbol{\xi}\rangle - \underline{\boldsymbol{T}}[\boldsymbol{x'}, t]\langle-\boldsymbol{\xi}\rangle) \cdot \boldsymbol{\eta}$ is the energy density in a bond and $w_c = \dfrac{4G_c}{\pi\delta^4}$ denotes the critical energy density.

In this work, the critical stretch and energy-based damage models are considered.

# Chapter 4

# Numerical Implementation

## 4.1 Discretization of Equations

At a material point $\boldsymbol{x}_k$, the discretized form of Eq. (2.31) is

$$\rho\,\ddot{\mathbf{u}}(\boldsymbol{x}_k,t)=\sum_{j=1}^{m}\left(\underline{\boldsymbol{T}}[\boldsymbol{x}_k,t]\langle\boldsymbol{x}_j-\boldsymbol{x}_k\rangle-\underline{\boldsymbol{T}}[\boldsymbol{x}_j,t]\langle\boldsymbol{x}_k-\boldsymbol{x}_j\rangle\right)(v_cV_j)+\boldsymbol{b}(\boldsymbol{x}_k,t)\,, \tag{4.1}$$

where $m$ denotes the total number of material points in the neighborhood of $\boldsymbol{x}_k$, $V_j$ the volume of material point $\boldsymbol{x}_j$ and $v_c$ is the volume correction factor for the material points lying on the limit of the neighborhood.

It is worth mentioning that, for each material point, the partial volumes of all its neighbors are computed and stored as an array. These partial volumes will then be retrieved by the appropriate routines for the computations of $\boldsymbol{K}$, $\boldsymbol{F}$ and the internal force density vector.

Furthermore, the shape tensor is approximated as

$$\boldsymbol{K}=\sum_{j=1}^{m}\omega(|\boldsymbol{x}_j-\boldsymbol{x}_k|)((\boldsymbol{x}_j-\boldsymbol{x}_k)\otimes(\boldsymbol{x}_j-\boldsymbol{x}_k))(v_cV_j) \tag{4.2}$$

Using the distributive property of the dyadic product and Eq. (2.30), the approximate deformation gradient tensor is evaluated as

$$\boldsymbol{F} = \left[ \sum_{j=1}^{m} \omega(|\boldsymbol{x}_j - \boldsymbol{x}_k|)((\boldsymbol{u}_j - \boldsymbol{u}_k) \otimes (\boldsymbol{x}_j - \boldsymbol{x}_k))(v_c V_j) \right] \boldsymbol{K}^{-1} + \boldsymbol{I} \,, \tag{4.3}$$

where $\boldsymbol{I}$ is the identity matrix.

## 4.2 Internal Force Density Computation

Within the context of quasi-static analysis with implicit time integration, the routine that evaluates the internal force density (IFD) vector is the principal component of a PD code.

For the implicit time integration, a nonlinear solver which uses the Newton-Raphson method calls the IFD routine for the tangent stiffness matrix assembly and the residual vector evaluation.

The internal force density routine is designed such that:

- The evaluation of $\underline{\boldsymbol{T}}[\boldsymbol{x}_k, t]$ is not repeated when computing the summation in Eq. (4.1). Hence, a direct approach to evaluating the summation may lead to incorrect entries in the IFD vector.

- The implementation accounts for potentially different material models at each material point in a bond.

The algorithm for the evaluation of the IFD vector is attached in the Appendix.

## 4.3 Tangent Stiffness Matrix Approximation

The tangent stiffness matrix (TSM) is crucial for the solution of nonlinear systems of equations using Newton-based methods. The entries of the TSM are approximated using the central difference method. The entries of $\boldsymbol{K}$ are defined as

$$K_{ij} = \frac{\partial f_i^{int}}{\partial u_j} \,, \tag{4.4}$$

where $f_i^{int}$ denotes the $i$-th component of the global IFD vector and $u_j$ the $j$-th component of the global displacement vector $\boldsymbol{u}$.

Based on the approach presented in [54], the following strategies were adopted:

- The entries in $\boldsymbol{K}$ are computed by means of the central difference method. The partial derivative in Eq. (4.4) is approximated as

$$K_{ij} \approx \frac{f_i^{int}(\boldsymbol{u} + \boldsymbol{\epsilon}^j) - f_i^{int}(\boldsymbol{u} - \boldsymbol{\epsilon}^j)}{2\epsilon}\,, \tag{4.5}$$

  where $\epsilon$ is the unique nonzero entry corresponding to the $j$-th degree of freedom in $\boldsymbol{\epsilon}^j$, the global perturbation vector.

- The perturbation value must be carefully chosen; it should be sufficiently small relative to the quantities of interest (in this case the displacement values) but not excessively small to avoid subtractive cancellation.

- The perturbed displacement vector is constructed based on the displacements of a material point and its neighbors only.

- A submatrix is used to account for the contribution of each material point into the global stiffness matrix $\boldsymbol{K}$ using a vector of global indices.

Despite the large body of literature on PD, the structural properties of $\boldsymbol{K}$ namely its sparsity pattern as well as its symmetry, are not fully understood. The current work aims to provide a deeper insight into the peridynamic tangent stiffness matrix.

## 4.4 Time Integration

When inertial effects are negligible, the problem is considered *quasi-static.* Therefore, Eq. (2.31) becomes

$$\int_H \{\underline{\boldsymbol{T}}[\boldsymbol{x},t]\langle \boldsymbol{x}'-\boldsymbol{x}\rangle - \underline{\boldsymbol{T}}[\boldsymbol{x}',t]\langle \boldsymbol{x}-\boldsymbol{x}'\rangle\}\,\mathrm{d}V_{\boldsymbol{x}'} + \boldsymbol{b}(\boldsymbol{x},t) = \boldsymbol{0} \tag{4.6}$$

In contrast to explicit methods, implicit methods are more stable despite their higher computational cost. Given that the governing equation Eq. (4.6) is a nonlinear function of displacement, the implicit integration scheme requires a nonlinear solver.

Eq. (4.6) is linearized as follows

$$\underbrace{\sum_{j=1}^{m} (\underline{\boldsymbol{T}}[\boldsymbol{x}_k,t]\langle \boldsymbol{x}_j-\boldsymbol{x}_k\rangle - \underline{\boldsymbol{T}}[\boldsymbol{x}_j,t]\langle \boldsymbol{x}_k-\boldsymbol{x}_j\rangle)(v_c V_j)}_{\boldsymbol{f}^{int}} + \underbrace{\boldsymbol{b}(\boldsymbol{x}_k,t)}_{\boldsymbol{f}^{ext}} = \boldsymbol{0} \tag{4.7}$$

$$\boldsymbol{f}^{int}(\boldsymbol{u}^n) + \underbrace{\left.\frac{\partial \boldsymbol{f}^{int}}{\partial \boldsymbol{u}}\right|_{\boldsymbol{u}^n}}_{\boldsymbol{K}(\boldsymbol{u}^n)} \Delta\boldsymbol{u} + \boldsymbol{f}^{ext} = \boldsymbol{0} \tag{4.8}$$

Therefore, at every iteration $n$, the following system of equations is solved

$$\boldsymbol{K}(\boldsymbol{u}^n)\,\boldsymbol{\Delta u} = -\boldsymbol{r}\,, \quad \boldsymbol{r} = \boldsymbol{f}^{int} + \boldsymbol{f}^{ext}\,, \tag{4.9}$$

where $\boldsymbol{K}$ denotes the TSM and $\boldsymbol{r}$ the residual vector.

An efficient and correct assembly of the $\boldsymbol{K}$ matrix is thus crucial for the solver to yield correct results.

Prior to the solution, specific operations must be carried out on the system in Eq. (4.9):

- When DBCs are enforced, if their values are zero, the contributions of the corresponding degrees of freedom (DOFs) are omitted, i.e., the appropriate rows and columns in $\boldsymbol{K}$ may be deleted or set to zero.

- The diagonal entries in $\boldsymbol{K}$ and the elements of the right-hand-side vector corresponding to the DOFs of nonzero DBC values are modified so as to stabilize the behavior of the system during the iteration process.

The standard Newton-Raphson method is in general *locally convergent*; its convergence rate is quadratic provided that the initial guess is close enough to the solution and that the Jacobian matrix is not ill-conditioned. However, in practice, these conditions may not be met due to the nature of the problems. As a result, the Newton-Raphson method may exhibit poor performance.

Given the aforementioned issues, the Newton-Raphson method is enhanced with a backtracking line search algorithm so as to achieve *global convergence* [55]. The next displacement iterate after solving Eq. (4.9) is therefore

$$\boldsymbol{u}^{n+1} = \boldsymbol{u}^{n} + \lambda \Delta \boldsymbol{u}\,, \tag{4.10}$$

where $\lambda$ is the line search parameter that adjusts the Newton step $\Delta\boldsymbol{u}$.

## 4.5 Solver Design

The solver is developed in C++ and exploits the main features of the language including data encapsulation, inheritance, polymorphism as well as dynamic memory allocation. The design is focused on minimal complexity, reduced number of dependencies, maintainability and extensibility. Specific computations and data processing are carried out by means of libraries and utilities. The architecture of the code is depicted in the Appendix.

### 4.5.1 Neighbor search

The meshfree nature of the discretization requires the construction of a neighbor list for each material point in the domain. Such an operation is crucial since the neighbor list will be used in all subsequent computations. Given the potentially large number of material points, the brute-force approach is inefficient since it has an $\mathcal{O}(N)$ time complexity, where $N$ is the size of the data; in this case, the total number of material points.

A more efficient approach is the use of space-partitioning data structures such as $k$-d trees for which the nearest neighbor search for all the material points takes $\mathcal{O}(logN)$ on average [56]. In this project, the neighbor search is carried out with the KDTREE2 library which implements a $k$-d tree algorithm on Euclidean spaces.

| **Tool** | **Functions** |
|---|---|
| Armadillo [57] | • Provides MATLAB®-like routines<br>• Used for constraint region generation |
| Boost | Provides auxiliary containers for data management |
| KDTREE2 [56] | • Implements a spatial data structure<br>• Used for neighbor list construction |
| PARDISO [58, 59, 60] | Used for the solution of linear systems |
| gnuplot-iostream | Used for data visualization |

Table 4.1: Dependencies of the solver

### 4.5.2 Representations of sparse matrices

Sparse matrices are often encountered in scientific and engineering problems during the numerical solution of differential equations. Given their structures - the number of nonzero elements is significantly smaller than the matrix size - it is essential to use appropriate data structures to store only the nonzero entries as well as particular algorithms to manipulate them.

#### 4.5.2.1 Storage schemes

Various storage schemes are available for sparse matrices including the Compressed Sparse Row (CSR), Compressed Sparse Column, Coordinate and Block Compressed Sparse Row formats. These storage schemes are *static data structures* since they are defined in terms of fixed-size arrays.

In contrast, *dynamic data structures* are more flexible due to run-time memory allocation. Vectors of the C++ Standard Template Library, linked lists and binary search trees are among the most common dynamic data structures.

In this project, the tangent stiffness matrix assembly is carried out in a two-stage process:

the incremental matrix assembly with a dynamic data structure followed by the conversion of the latter into the more compact CSR format.

#### 4.5.2.2 Incremental matrix assembly

The approach adopted herein is similar to that proposed by Jansson [61] who proposed a stack-based representation for sparse matrix assembly. In this project, the tangent stiffness matrix is populated by means of a *hash table*. To reduce the complexity of the implementation, the hash table is implemented as an array of singly linked lists. The data structure has been designed such that *only* the nonzero elements are stored.

The output of the assembly, after the necessary modifications, is the global stiffness matrix stored in the CSR3 format.

The latter consists of three arrays:

- Let $n$ denote the number of rows of the square matrix and $nnz$ the number of nonzero entries. $\boldsymbol{a}$ is an array of length $nnz$ that stores the nonzero entries.
- $\boldsymbol{ja}$ is an array of length $nnz$ which stores the column indices of the nonzero entries in the original matrix.
- $\boldsymbol{ia}$ is an array of length $n+1$ which stores the indices in $\boldsymbol{a}$ corresponding to the first nonzero entries in each row. It is noted that the last element in $\boldsymbol{ia}$ must be $nnz$ and that the number of nonzero entries per row is $ia[i+1] - ia[i], \quad i = 0, \cdots, n$, following a zero-based indexing.

For example, given a sparse matrix $\boldsymbol{A}$

$$\boldsymbol{A} = \begin{pmatrix} 1 & -1 & 0 & -3 \\ -2 & 5 & 0 & 0 \\ 0 & 0 & 4 & 6 \\ -4 & 0 & 0 & 7 \end{pmatrix}$$

Using the zero-based indexing, the CSR3 representation of $\boldsymbol{A}$ is thus

$$\begin{aligned}
\boldsymbol{a} &= \begin{pmatrix} 1 & -1 & -3 & -2 & 5 & 4 & 6 & -4 & 7 \end{pmatrix}, \\
\boldsymbol{ja} &= \begin{pmatrix} 0 & 1 & 3 & 0 & 1 & 2 & 3 & 0 & 3 \end{pmatrix}, \\
\boldsymbol{ia} &= \begin{pmatrix} 0 & 3 & 5 & 7 & 9 \end{pmatrix}
\end{aligned}$$

# Chapter 5

# Discussion and Conclusion

## 5.1 Discussion

Various features of the peridynamic theory have been considered within the scope of the current work. Notably, the enforcement of BCs is one of the most challenging aspects of the problem considering the nature of the formulation; constraints are applied through material layers. Since the minimum thickness of the constraint region (Fig. (2.4)) is the horizon size, there is no restriction on the number of material points within the constraint regions. Therefore, the total number of DOFs in the system depends on the implementation. For the aforementioned reasons, the performance of a PD solver may be improved by exploiting the symmetry of the geometry whenever applicable [62].

Since PD simulations are computationally expensive, it is necessary to implement techniques that reduce storage requirements and computation time. For instance, a knowledge of the features of the TSM can be exploited to boost the efficiency of the solver; if the TSM possesses *numerical symmetry*, only its upper or lower triangular part needs to be stored and passed to the linear solver. The TSM assembly is a major bottleneck during the simulation given the method used to compute its entries along with the required modifications prior to the solution of the linear system of equations. Therefore, *cache-friendly* data structures should be used to store the sparse matrix; for example, containers with contiguous memory storage. Furthermore, parallelization is required for all practical applications to render the simulations less expensive. Moreover, preallocation of the TSM may be advantageous.

It is also noted that more advanced algorithms may be used for the volume correction procedure, at the expense of increased complexity [63]. It has been demonstrated that the volume correction procedure greatly affects the convergence of the solution [64, 63].

On the physical significance of the horizon, it is worth mentioning that, at the macroscale, a material modeled with the peridynamic formulation is assumed to possess an underlying microstructure [65] since the interactions between the material points within a body need not be physically meaningful; the horizon is a mathematical quantity that appears in the governing equation and may be calibrated with other parameters including grid spacing to reproduce the material properties. However, the horizon $\delta$ must reflect the appropriate length scale dictated by the physics of the problem; nonlocal effects are prominent for problems including nanoscale structures and fracture [66].

Figure 5.1 illustrates the deformation of a unit cube calculated by the peridynamic code developed here subjected to a displacement loading of magnitude $d = 0.2$ along its front face and fixed along its back face. The material parameters are $E = 2.5$ and $\nu = 0.45$. The cube is discretized into 25 material points along each edge and the horizon size is chosen such that $\delta = 1.5\,\Delta$.

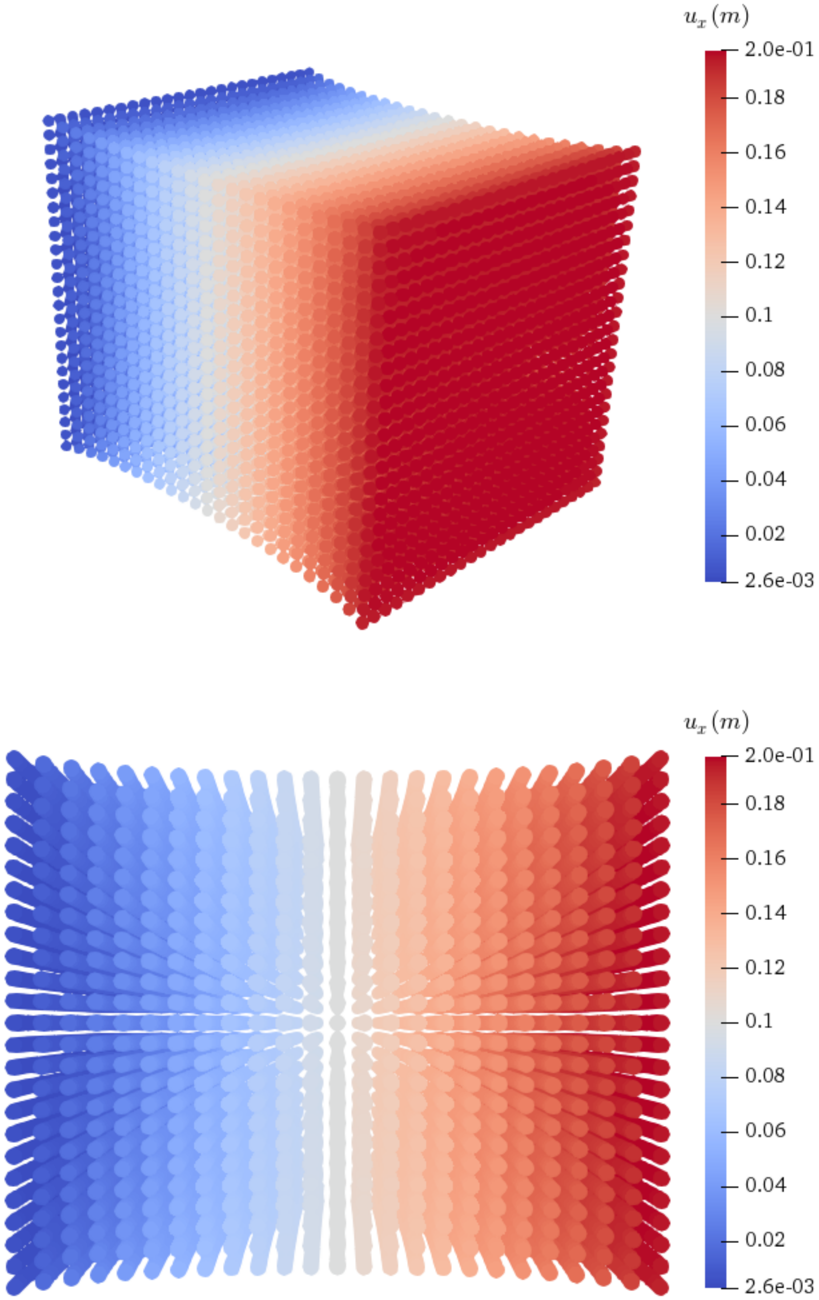

Figure 5.1: Cube under tension

## 5.2 Concluding Remarks

The present work is concerned with providing a deeper insight into the NOSB-PD formulation and its numerical implementation. A Lagrangian, object-oriented application has been developed in order to simulate structural responses under quasi-static loading conditions. Since CCM material models can be directly incorporated in to the NOSB-PD formulation, the Neo-Hookean hyperelastic material model is used, aiming to investigate the large deformations of a peridynamic continuum. The aforementioned test case, despite the coarse discretization, illustrates promising capabilities of the solver, i.e., hyperelastic deformations may be captured by the NOSB-PD formulation and there is no restriction on the material properties.

In contrast to the bond-based and ordinary state-based formulations, the NOSB-PD formulation does not require the estimation of *surface correction factors*; however, in its original form, the NOSB-PD formulation suffers from zero-energy mode instabilities due to the erroneous computation of the approximate deformation gradient tensor. Their effects are suppressed by adding a stabilizing term to the force state expression.

The numerous aspects of the numerical implementation namely the boundary conditions, TSM assembly, volume correction procedures have been addressed and multiple strategies have been proposed to enhance the performance of the solver.

## 5.3 Outlook

From the preliminary results of the test case, a thorough investigation of structural responses under different loading conditions will be examined. Notably, finite deformations will be investigated and comparisons of PD solutions with those from the FEM will be carried out.

Furthermore, it is aimed to design a more efficient pre-processor and post-processor. In particular, the pre-processor is required to process the user-defined input data and generate the peridynamic grid along with the constraint regions accordingly.

Moreover, the investigation of crack initiation and propagation for quasi-static as well as dynamic loading conditions is envisaged. In that regard, a dynamic solver will be implemented as future work.

Also, it is desired to boost the performance and enhance efficiency of the program by using different quadrature rules as well as implementing adequate parallelization strategies.

In addition, given the object-oriented nature of the language, it is aimed to implement different types of constitutive and damage models to analyze various structural responses.

Ideally, the current code is to be coupled with a finite element solver so that potential damage initiation and propagation will be confined within the PD domain and the remainder of the domain is treated with the FEM.

# Bibliography

[1] C. E. Inglis, “Stresses in a plate due to the presence of cracks and sharp corners,” *Transactions of the Institute of Naval Architects*, vol. 55, pp. 219–242, 1913.

[2] A. A. Griffith, “The phenomena of rupture and flow in solids,” *Philosophical Transactions of the Royal Society of London A: Mathematical, Physical and Engineering Sciences*, vol. 221, no. 582–593, pp. 163–198, 1921.

[3] E. Madenci and E. Oterkus, *Peridynamic theory and its applications.* Springer, 2014.

[4] G. I. Barenblatt, “The formation of equilibrium cracks during brittle fracture: General ideas and hypotheses,” *Applied Mathematics and Mechanics*, vol. 23, no. 3, pp. 622–636, 1959.

[5] G. I. Barenblatt, “The mathematical theory of equilibrium cracks in brittle fracture,” *Advances in Applied Mechanics*, vol. 7, pp. 55–129, 1962.

[6] D. Dugdale, “Yielding of steel sheets containing slits,” *Journal of the Mechanics and Physics of Solids*, vol. 8, no. 2, pp. 100 – 104, 1960.

[7] A. Needleman, “A continuum model for void nucleation by inclusion debonding,” *Journal of Applied Mechanics*, vol. 54, pp. 525 – 531, 1987.

[8] T. Belytschko and T. Black, “Elastic crack growth in finite elements with minimal remeshing,” *International Journal for Numerical Methods in Engineering*, vol. 45, pp. 601–620, 1999.

[9] J. M. Melenk and I. Babuška, “The partition of unity finite element method: Basic

theory and applications," *Computer Methods in Applied Mechanics and Engineering*, vol. 139, no. 1-4, pp. 289–314, 1996.

[10] V. Chiaruttini, D. Geoffroy, V. Riolo, and M. Bonnet, "An adaptive algorithm for cohesive zone model and arbitrary crack propagation," *European Journal of Computational Mechanics*, vol. 21, pp. 208–218, 2012.

[11] G. Zi, T. Rabczuk, and W. Wall, "Extended meshfree methods without branch enrichment for cohesive cracks," *Computational Mechanics*, vol. 40, no. 2, pp. 367–382, 2007.

[12] A. C. Eringen, "Nonlocal polar elastic continua," *International Journal of Engineering Science*, vol. 10, no. 1, pp. 1 – 16, 1972.

[13] A. C. Eringen and D. G. B. Edelen, "On nonlocal elasticity," *International Journal of Engineering Science*, vol. 10, no. 3, pp. 233 – 248, 1972.

[14] S. A. Silling, "Reformulation of elasticity theory for discontinuities and long-range forces," *Journal of the Mechanics and Physics of Solids*, vol. 48, no. 1, pp. 175–209, 2000.

[15] S. A. Silling, M. Epton, O. Weckner, J. Xu, and E. Askari, "Peridynamic states and constitutive modeling," *Journal of Elasticity*, vol. 88, no. 2, pp. 151–184, 2007.

[16] A. Javili, R. Morasata, E. Oterkus, and S. Oterkus, "Peridynamics review," *Mathematics and Mechanics of Solids*, 2018.

[17] W. Liu and J.-W. Hong, "Discretized peridynamics for brittle and ductile solids," *International Journal for Numerical Methods in Engineering*, vol. 89, no. 8, pp. 1028–1046, 2012.

[18] Y. le Hu, Y. Yu, and H. Wang, "Peridynamic analytical method for progressive damage in notched composite laminates," *Composite Structures*, vol. 108, pp. 801 – 810, 2014.

[19] S. Oterkus, E. Madenci, and A. Agwai, "Peridynamic thermal diffusion," *Journal of Computational Physics*, vol. 265, pp. 71–96, 2014.

[20] T. L. Warren, S. A. Silling, A. Askari, O. Weckner, M. A. Epton, and J. Xu, "A non-ordinary state-based peridynamic method to model solid material deformation and fracture," *International Journal of Solids and Structures*, vol. 46, no. 5, pp. 1186–1195, 2009.

[21] J. T. Foster, S. A. Silling, and W. W. Chen, "Viscoplasticity using peridynamics," *International Journal for Numerical Methods in Engineering*, vol. 81, no. 10, pp. 1242–1258, 2010.

[22] M. Tupek, J. Rimoli, and R. Radovitzky, "An approach for incorporating classical continuum damage models in state-based peridynamics," *Computer Methods in Applied Mechanics and Engineering*, vol. 263, pp. 20 – 26, 2013.

[23] J. Amani, E. Oterkus, P. Areias, G. Zi, T. Nguyen-Thoi, and T. Rabczuk, "A non-ordinary state-based peridynamics formulation for thermoplastic fracture," *International Journal of Impact Engineering*, vol. 87, pp. 83–94, 2016.

[24] "A non-ordinary state-based peridynamics modeling of fractures in quasi-brittle materials," *International Journal of Impact Engineering*, vol. 111, pp. 130 – 146, 2018.

[25] V. P. Nguyen, T. Rabczuk, S. Bordas, and M. Duflot, "Meshless methods: A review and computer implementation aspects," *Mathematics and Computers in Simulation*, vol. 79, no. 3, pp. 763 – 813, 2008.

[26] Y. Chen, J. Lee, and A. Eskandarian, *Meshless methods in solid mechanics.* Springer, 2006.

[27] Y. Gu, C. Yan, and P. K. Yarlagadda, "An advanced meshless technique for large deformation analysis of metal forming," in *9th Global Congress on Manufacturing and Management* (P. K. Yarlagadda and P. V. Gudimetla, eds.), Global Congress on Manufacturing and Management (GCMM) Board, November 2008.

[28] E. Cueto and F. Chinesta, "Meshless methods for the simulation of material forming," *International Journal of Material Forming*, vol. 8, 03 2013.

[29] D. A. Hu, X. Han, and S. Y. Long, "A modified meshless local petrov-galerkin method

for nearly incompressible rubber materials," in *Computational Mechanics*, (Berlin, Heidelberg), pp. 339–339, Springer Berlin Heidelberg, 2009.

[30] T. Douillet-Grellier, B. D. Jones, R. Pramanik, K. Pan, A. Albaiz, and J. R. Williams, "Mixed-mode fracture modeling with smoothed particle hydrodynamics," *Computers and Geotechnics*, vol. 79, pp. 73 – 85, 2016.

[31] X. Zhuang, C. Augarde, and S. Bordas, "Accurate fracture modelling using meshless methods, the visibility criterion and level sets: Formulation and 2d modelling," *International Journal for Numerical Methods in Engineering*, vol. 86, no. 2, pp. 249–268, 2011.

[32] M. Marder, "Particle methods in the study of fracture," *International Journal of Fracture*, vol. 196, no. 1, pp. 169–188, 2015.

[33] S. Silling, "Dynamic fracture modeling with a meshfree peridynamic code," in *Computational Fluid and Solid Mechanics 2003* (K. Bathe, ed.), pp. 641 – 644, Oxford: Elsevier Science Ltd, 2003.

[34] M. L. Parks, R. B. Lehoucq, S. J. Plimpton, and S. A. Silling, "Implementing peridynamics within a molecular dynamics code," *Computer Physics Communications*, vol. 179, no. 11, pp. 777–783, 2008.

[35] Sandia National Laboratories, *LAMMPS users manual*, 2003.

[36] R. W. Macek and S. A. Silling, "Peridynamics via finite element analysis," *Finite Elements in Analysis and Design*, vol. 43, no. 15, pp. 1169–1178, 2007.

[37] M. L. Parks, D. J. Littlewood, J. A. Mitchell, and S. A. Silling, "Peridigm users' guide," Tech. Rep. Report SAND2012-7800, 2012.

[38] A. Javili, A. McBride, and P. Steinmann, "Continuum-kinematics-inspired peridynamics. mechanical problems," *Journal of the Mechanics and Physics of Solids*, vol. 131, pp. 125 – 146, 2019.

[39] S. A. Silling and E. Askari, "A meshfree method based on the peridynamic model of solid mechanics," *Computers and Structures*, vol. 83, no. 17-18, pp. 1526–1535, 2005.

[40] "Peridynamic formulations enriched with bond rotation effects," *International Journal of Engineering Science*, vol. 121, pp. 118 – 129, 2017.

[41] D. Han, Y. Zhang, Q. Wang, W. Lu, and B. Jia, "The review of the bond-based peridynamics modeling," *Journal of Micromechanics and Molecular Physics*, 2018.

[42] Y. Hu and E. Madenci, "Bond-based peridynamics with an arbitrary Poisson's ratio," in *57th AIAA/ASCE/AHS/ASC Structures, Structural Dynamics, and Materials Conference*, 2016.

[43] C. Diyaroglu, E. Oterkus, S. Oterkus, and E. Madenci, "Peridynamics for bending of beams and plates with transverse shear deformation," *International Journal of Solids and Structures*, vol. 69–70, pp. 152–168, 2015.

[44] W. Zhou and D. Liu, "A peridynamic model for analyzing crack propagation in unidirectional composite lamina," in *Proceedings of the American Society for Composites - 31st Technical Conference, ASC 2016*, 2016.

[45] P. Seleson and M. Parks, "On the role of the influence function in the peridynamic theory," *International Journal for Multiscale Computational Engineering*, vol. 9, no. 6, pp. 689–706, 2011.

[46] S. Silling, "Stability of peridynamic correspondence material models and their particle discretizations," *Computer Methods in Applied Mechanics and Engineering*, vol. 322, pp. 42 – 57, 2017.

[47] M. S. Breitenfeld, *Quasi-static non-ordinary state-based peridynamics for the modeling of 3D fracture.* PhD thesis, University of Illinois at Urbana-Champaign, 2014.

[48] A. Yaghoobi and M. G. Chorzepa, "Higher-order approximation to suppress the zero-energy mode in non-ordinary state-based peridynamics," *Computers & Structures*, vol. 188, pp. 63–79, 2017.

[49] P. Li, Z. Hao, and W. Zhen, "A stabilized non-ordinary state-based peridynamic model," *Computer Methods in Applied Mechanics and Engineering*, vol. 339, pp. 262 – 280, 2018.

[50] X. Gu, E. Madenci, and Q. Zhang, "Revisit of non-ordinary state-based peridynamics,"

*Engineering Fracture Mechanics*, vol. 190, pp. 31 – 52, 2018.

[51] F. Bobaru, Y. D. Ha, and W. Hu, “Numerical integration in peridynamics,” tech. rep., University of Nebraska-Lincoln, 2010.

[52] Q. V. Le and F. Bobaru, “Surface corrections for peridynamic models in elasticity and fracture,” *Computational Mechanics*, vol. 61, no. 4, pp. 499–518, 2018.

[53] J. Foster, S. A. Silling, and W. Chen, “An energy based failure criterion for use with peridynamic states,” *International Journal for Multiscale Computational Engineering*, vol. 9, no. 6, pp. 675–688, 2011.

[54] D. J. Littlewood, “Roadmap for peridynamic software implementation,” Tech. Rep. SAND2015-9013, Sandia National Laboratories, Albuquerque, New Mexico, 2015.

[55] R. B. S. J. E. Dennis, *Numerical methods for unconstrained optimization and nonlinear equations.* Classics in applied mathematics 16, Society for Industrial and Applied Mathematics, 1987.

[56] M. Kennel, “KDTREE 2: Fortran 95 and c++ software to efficiently search for near neighbors in a multi-dimensional euclidean space,” 09 2004.

[57] C. Sanderson and R. Curtin, “Armadillo: a template-based C++ library for linear algebra,” *Journal of Open Source Software*, vol. 1, p. 26, 2016.

[58] A. De Coninck, B. De Baets, D. Kourounis, F. Verbosio, O. Schenk, S. Maenhout, and J. Fostier, “Needles: Toward large-scale genomic prediction with marker-by-environment interaction,” vol. 203, no. 1, pp. 543–555, 2016.

[59] F. Verbosio, A. D. Coninck, D. Kourounis, and O. Schenk, “Enhancing the scalability of selected inversion factorization algorithms in genomic prediction,” *Journal of Computational Science*, vol. 22, no. Supplement C, pp. 99 – 108, 2017.

[60] D. Kourounis, A. Fuchs, and O. Schenk, “Towards the next generation of multiperiod optimal power flow solvers,” *IEEE Transactions on Power Systems*, vol. PP, no. 99, pp. 1–10, 2018.

[61] N. Jansson, “Optimizing sparse matrix assembly in finite element solvers with one-sided communication,” in *VECPAR*, 2012.

[62] A. Yaghoobi and M. G Chorzepa, “Formulation of symmetry boundary modeling in non-ordinary state-based peridynamics and coupling with finite element analysis,” *Mathematics and Mechanics of Solids*, p. 108128651771149, 2017.

[63] P. Seleson, “Improved one-point quadrature algorithms for two-dimensional peridynamic models based on analytical calculations,” *Computer Methods in Applied Mechanics and Engineering*, vol. 282, pp. 184 – 217, 2014.

[64] “Convergence studies in meshfree peridynamic simulations,” *Computers & Mathematics with Applications*, vol. 71, no. 11, pp. 2432 – 2448, 2016.

[65] S. N. Butt and G. Meschke, “Wave dispersion and propagation in a linear peridynamic solid,” *PAMM*, vol. 17, no. 1, pp. 409–410, 2017.

[66] S. A. Silling and R. B. Lehoucq, “Convergence of peridynamics to classical elasticity theory,” *Journal of Elasticity*, vol. 93, no. 1, p. 13, 2008.

# Appendix A

# Sample input file

Listing A.1: Input file structure

```
#/*Copyright (C) 2019. Rico Morasata. All rights reserved.*/

#This is an input file for a peridynamics case study.
#The geometry is a rectangular plate with a hole at its center.
#The quantities involved in the analysis are assumed to be in SI units.
#The input file is structured in the subsequent manner:

#Define domain dimensions
Dimensions
        geometry_type = plate_with_cutout
        length = 0.05
        width = 0.05
        thickness = 0.0005
        diameter = 0.01
End dimensions

Material properties
        E = 192e9
        nu = 0.333
        rho  = 8000
End material properties

Spatial discretization
        Divisions_along_x = 50
        Divisions_along_y = 50
        Spacing_between_points = 0.001
        Horizon_size_factor = 3.015
End spatial discretization

#Specify boundary conditions: constraints(velocity and/or displacement) and/or force.
#Free edge is also a boundary condition.
Top edge
        Type = velocity
        V_x = 0
        V_y = 2.7541e−7
End top edge

Bottom edge
        Type = velocity
        V_x = 0
        V_y = −2.7541e−7
End bottom edge
```

```
Left edge
        Type = free
End left edge

Right edge
        Type = free
End right edge

#Specify initial conditions on interior points
#Initial displacement gradient
#       Displacement_gradient = 0  0  0  0
#End initial displacement gradient

#Initial velocity gradient
#       Velocity_gradient = 0  0  0  0
#End initial velocity gradient

#Define analysis type. A quasistatic analysis is carried out via implicit time integration
Analysis
        Analysis_type          = quasistatic
        Consitutive_model      = saint_venant_kirchhoff
        Damage_model           = critical_stretch
        Damage_parameter       = 0.02
        Time_step              = 1
        Total_number_of_steps = 1000
End analysis
```

**Algorithm 1** Routine for computing the global internal force density vector for the NOSB-PD formulation

```
▷ Initialize the force vector to zero
for each material point $i$ do
    $\boldsymbol{f}_i = \mathbf{0}$
end for
▷ Compute $\boldsymbol{K}^{-1}$ and $\boldsymbol{F}$
for each material point $i$ do                              ▷ loop over all the material points
    $\boldsymbol{K} \leftarrow \mathbf{0}$
    $\boldsymbol{F} \leftarrow \mathbf{0}$
    for each material point $j$ in the neighborhood of $i$ do
        $d_{ij} \in \{0.0, 1.0\}$                           ▷ 0.0 if the bond is broken and 1.0 if intact
        $\boldsymbol{\xi} \leftarrow \boldsymbol{x}_j - \boldsymbol{x}_i$
        $\boldsymbol{\eta} \leftarrow \boldsymbol{u}_j - \boldsymbol{u}_i$
        $\omega \leftarrow \omega(|\boldsymbol{\xi}|)$                                 ▷ Evaluate influence function
        $\boldsymbol{K} \leftarrow \boldsymbol{K} + (d_{ij}\, v_c\, \Delta V_j)(\boldsymbol{\xi} \otimes \boldsymbol{\xi})$       ▷ $v_c$ is a volume correction factor
        $\boldsymbol{H} \leftarrow \boldsymbol{H} + (d_{ij}\, v_c\, \Delta V_j)(\boldsymbol{\eta} \otimes \boldsymbol{\xi})$       ▷ $\boldsymbol{H}$ is an auxiliary tensor
    end for
    $\boldsymbol{F} \leftarrow \boldsymbol{H}\boldsymbol{K}^{-1} + \boldsymbol{I}$              ▷ $\boldsymbol{I}$ is the second-order identity tensor
end for
▷ Compute pairwise contributions to the global internal force density vector
for each material point $i$ do                              ▷ loop over all the material points
    for each material point $j$ in the neighborhood of $i$ do
        $\boldsymbol{\xi} \leftarrow \boldsymbol{x}_j - \boldsymbol{x}_i$
        $\boldsymbol{S} = \partial W(\boldsymbol{E})/\partial \boldsymbol{E}$            ▷ Obtain $\boldsymbol{S}$ from a hyperelastic material model
        $\boldsymbol{P} = \boldsymbol{F}\boldsymbol{S}$
        $\underline{\boldsymbol{T}}\langle\boldsymbol{\xi}\rangle = \omega(|\boldsymbol{\xi}|)\, \boldsymbol{P}\, \boldsymbol{K}^{-1}\, \boldsymbol{\xi}$                  ▷ Stabilization term is optional
        $\boldsymbol{f}_i \leftarrow \boldsymbol{f}_i + d_{ij}\, v_c\, \Delta V_j\, \underline{\boldsymbol{T}}\langle\boldsymbol{\xi}\rangle$
        $\boldsymbol{f}_j \leftarrow \boldsymbol{f}_j - d_{ij}\, v_c\, \Delta V_i\, \underline{\boldsymbol{T}}\langle\boldsymbol{\xi}\rangle$
    end for
end for
```

**Algorithm 2** Routine for the tangent stiffness matrix assembly by means of the central difference method

```
Require: $\varepsilon$                                        ▷ value of the perturbation parameter
Require: $n_{DOFs}$                                           ▷ total number of DOFs in the system
Require: an instance of a class that implements a dynamic data structure. Its constructor
    takes $n_{DOFs}$ as argument.
    ▷ Loop over all material points
for each material point $i$ in the domain do
    Construct the "transversal list" consisting of material point $i$ and all its neighbors
    Let $m$ denote the size of the "transversal list"
    Define a vector of global indices of size $2m$
    Allocate a "local stiffness matrix" $\boldsymbol{K_{local}}$ of size $2m \times 2m$
    for each material point $j$ in the "transversal list" do
        for each displacement DOF $c$ at material point $j$ do
            Let $\boldsymbol{u}$ denote the displacement of material point $j$
            $u[c] \mathrel{+}= \varepsilon$                    ▷ Apply positive perturbation
    ▷ Compute the subset of the internal force density vector
    ▷ Let $\boldsymbol{f}_{int}^{+\varepsilon}$ and $\boldsymbol{f}_{int}^{-\varepsilon}$ be vectors of size $2m$
            Update auxiliary tensors at $i$
            Compute force state at $i$ under positive perturbation
            $\underline{\boldsymbol{T}}^{+\varepsilon}\langle\boldsymbol{\xi}\rangle = \omega(|\boldsymbol{\xi}|)\,\boldsymbol{P}_i\,\boldsymbol{K}_i^{-1}\,\boldsymbol{\xi}$
            Evaluate $\boldsymbol{f}_{int}^{+\varepsilon}$ as per Algorithm 1
            Restore the unperturbed value of the entry in $\boldsymbol{u}$
            $u[c] \mathrel{-}= \varepsilon$                    ▷ Apply negative perturbation
            Repeat the aforementioned steps and compute $\boldsymbol{f}_{int}^{-\varepsilon}$
            Restore the unperturbed value of the entry in $\boldsymbol{u}$
            Fill $\boldsymbol{K_{local}}$ column-wise with the tangent values
            for $k \leftarrow 0$ to $m - 1$ do
                for $d \leftarrow 0$ to $2$ do
                    $K_{local}[2k+d][2j+c] = (f_{int}^{+\varepsilon}[2k+d] - f_{int}^{-\varepsilon}[2k+d])/2\varepsilon$
                end for
            end for
        end for
    end for
    Place $\boldsymbol{K_{local}}$ into $\boldsymbol{K}$ using the vector of global indices    ▷ $\boldsymbol{K}$ is the global stiffness
    matrix
end for
Modify $\boldsymbol{K}$ to reflect the BCs
Convert the dynamic data structure into the CSR3 storage format
```

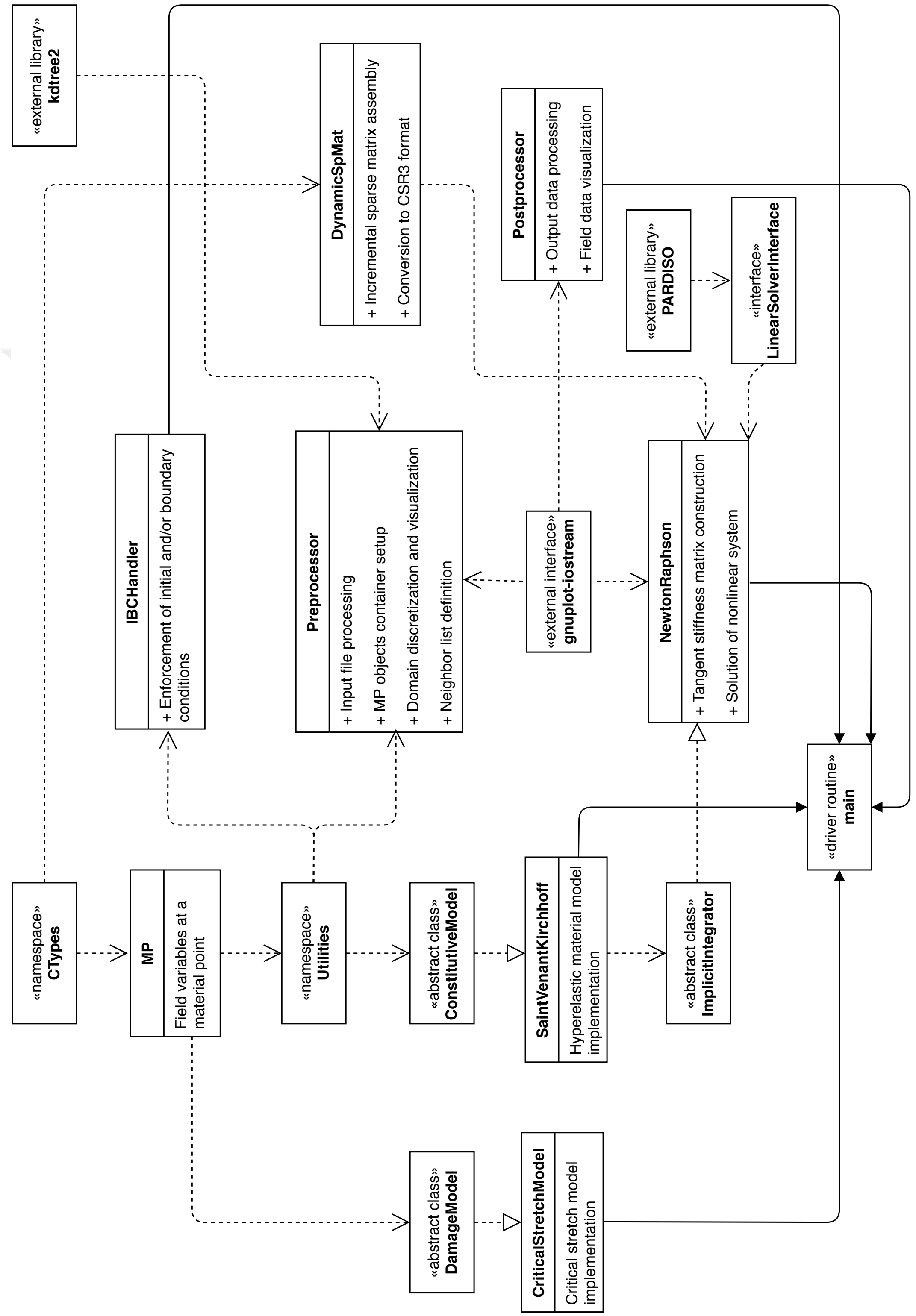

Figure A.1: Solver architecture